Polymer 366 (2026) 130758

Contents lists available at ScienceDirect

Polymer

journal homepage: www.elsevier.com/locate/polymer

Phase behavior of linear-branched block copolymers with precisely controlled branch-point positions

Tianyu Zheng [a,1], Juntong He [a,1], Zhanhui Gan [a], Jinbin Li [a], Zhuang Ma [b,*], Jiajia Zhou [a,c,**], Xue-Hui Dong [a,c,***]

[a] South China Advanced Institute for Soft Matter Science and Technology, School of Emergent Soft Matter, South China University of Technology, Guangzhou, 510640, China
[b] Institute of Materials Intelligent Technology, Liaoning Academy of Materials, Shenyang, 110004, China
[c] Guangdong Provincial Key Laboratory of Functional and Intelligent Hybrid Materials and Devices, South China University of Technology, Guangzhou, 510640, China

ARTICLE INFO

Keywords:
Block copolymer
Self-assembly
Architecture
Branching
Frank-Kasper phases

ABSTRACT

Precisely positioning a single branch-point within the A-block of compositionally invariant AB diblock copolymers provides an orthogonal design handle to program long-range ordered nanostructures. In this work, we synthesized a library of linear-branched architectures in which the branching location shifts from the free A terminus toward the A/B junction. Small-angle X-ray scattering (SAXS) indicates that this topological variation triggers phase transitions among a range of ordered phases, including hexagonally packed cylinders (HEX), body-centered cubic (BCC) spheres, and Frank-Kasper σ phase. Self-consistent field theory (SCFT) reveals that the spatial distribution of branch segments modulates both the effective interfacial curvature and the entropic penalty of chain stretching, thereby stabilizing different ordered states. These results underscore branching location as a decisive and independent design parameter for block copolymer self-assembly, offering a route to access complex mesophases without altering composition or chain length.

1. Introduction

Block copolymers consisting of two or more chemically distinct polymer blocks are well-known to self-assemble into a rich array of equilibrium nanostructures, including body-centered cubic (BCC) spheres, hexagonally packed cylinders (HEX), bicontinuous double gyroids (DG), and lamellae (LAM) [1–3]. These morphologies arise from the interplay of thermodynamic parameters (Flory-Huggins interaction parameter χ) and geometric parameters (total molecular weight N and block volume fraction f), which collectively balance interfacial energy and chain conformational entropy [4]. Moreover, the architecture of block copolymers plays a pivotal role in directing self-assembly [5–9]. Notably, architectural variations (*e.g.*, branched, star, cyclic, *etc.*) introduce unique spatial constraints that redefine the local packing symmetry [10–16]. These constraints alter the competition among free energy contributions, enabling access to non-classical phases that are usually difficult to capture in linear systems [17–24].

Branching is among the most synthetically accessible and topologically versatile architectures, exhibiting rich self-assembly behaviors that depend critically on the branch-point location [20–22,25]. In most conventional linear-branched structures, the branch point coincides with the A/B junction where chemically dissimilar blocks are connected. The branching architecture increases conformational asymmetry [18,20]. This asymmetry is quantified by $\varepsilon = x_B b_A / x_A b_B$, where x_i denotes the branching numbers of the block i and b_i is the Kuhn length ($x_i = 1$ for a linear diblock copolymer) [17,18]. Strong conformational asymmetry (*e.g.*, $\varepsilon \gg 1$) disrupts symmetric chain stretching, expands the spherical phase region and stabilizes non-classical lattices such as Frank-Kasper

This article is part of a special issue entitled: POLYMER Rising Star 2026 published in Polymer.

* Corresponding author.Institute of Materials Intelligent Technology, Liaoning Academy of Materials, Shenyang, 110004, China
** Corresponding author.South China Advanced Institute for Soft Matter Science and Technology, School of Emergent Soft Matter, South China University of Technology, Guangzhou, 510640, China
*** Corresponding author.South China Advanced Institute for Soft Matter Science and Technology, School of Emergent Soft Matter, South China University of Technology, Guangzhou 510640, China
E-mail addresses: zma@lam.ln.cn (Z. Ma), zhouj2@scut.edu (J. Zhou), xdong@scut.edu.cn (X.-H. Dong).
[1] These authors contributed equally to this work.

https://doi.org/10.1016/j.polymer.2026.130758
Received 30 July 2026; Received in revised form 26 August 2026; Accepted 31 August 2026
Available online 1 September 2026
0032-3861/© 2026 Elsevier Ltd. All rights are reserved, including those for text and data mining, AI training, and similar technologies.

phases [17,18,26]. Moreover, arms of non-equivalent lengths can also be deliberately designed to yield asymmetric branching [20,22]. Such combinations alleviate packing frustration—a thermodynamic penalty arising from the competition between the preference of maintaining spherical shapes for uniform stretching and the requirement for space filling without voids [20,22,27,28].

In contrast, when the branch point is embedded within one domain rather than on the A/B junction (*i.e.*, intra-domain branching), it no longer couples directly to interfacial curvature [21,29,30]. Instead, the branch segment imposes steric hindrance, perturbing local chain packing within the domain and altering conformational entropy [8,31]. The effect of such intradomain branching is less predictable and often leads to unexpected structural outcomes. Zhao et al. demonstrated linear-star block copolymers with a dynamic rotaxane-based branching unit which allows repositioning of the branch-point location within the same domain [29]. This system exhibits adaptive topological locking that markedly alters spinodal stability and leads to nonclassical phase sequences, highlighting how branching away from the interface can lead to unique and often unanticipated assembly pathways. Tuning the branch-point location along the backbone thus enables efficient manipulation of energy landscape, providing a robust route to unconventional phases.

Despite these opportunities, precise control over the branching position remains a synthetic challenge. Traditional polymerization suffers from stochastic chain growth, leading to inherent chain length polydispersity and poorly defined branch-point location [25,32–34]. These synthetic barriers have hindered systematic studies on the effects of branch-point location, leaving this area largely underexplored. In this study, we designed linear-branched block copolymers based on discrete oligo lactide (*o*LA) and oligo 2-hydroxytridecanoic acid (*o*DA) with exact chemical structures and uniform chain length. Leveraging the divergent and convergent synthetic approach, we achieved precise control over branch-point location and realized architectural evolution from linear-branched to linear-linear systems (Scheme 1). This positional variation induced sequential phase transitions from spheres to cylinders and finally to the Frank-Kasper σ phase. Self-consistent field theory (SCFT) calculations confirmed that the branch-point location modulates the spatial distribution of the branch segment, thereby tuning the balance between interfacial curvature and chain stretching entropy.

2. Results and discussion

The designed block copolymers, denoted as L_{n1} (L_{nT})L_{n2}-DA, consist of a branched L block and a linear DA block (Fig. 1a). In this architecture, $L_{n1}L_{n2}$ constitutes the main chain, whereas the short L_{nT} segment ($n_T = 8$) is defined as the branch segment. Discrete L and DA homopolymers were prepared by iterative exponential growth (Schemes S1 and S2) [33]. A Y-shaped molecular adaptor bearing two activated hydroxyls and one latent carboxyl group served as the branch point. Successive esterification stitched three L segments together to form the exact branched architecture. After removing the benzyl protecting group, a DA block was installed, affording the designed block copolymers.

The attachment site of the branch segment on the L main chain is defined as the branch point, while the L/DA connection is denoted as the A/B junction. A series of branched block copolymers with varying branch-point position was prepared. A dimensionless parameter $\tau = n_1/(n_1 + n_2)$ was introduced to characterize the complex branched configuration of the isomers (Scheme 1). When $\tau = 1$, the branched point coincides with the A/B junction, corresponding to interfacial branching and an asymmetric linear-branched architecture (Scheme 1). As τ decreases, the branch point gradually shifts away from the A/B junction along the L main chain; $\tau = 0$ corresponds to the linear-linear analogue without the branch segment. Detailed molecular information is summarized in Table 1.

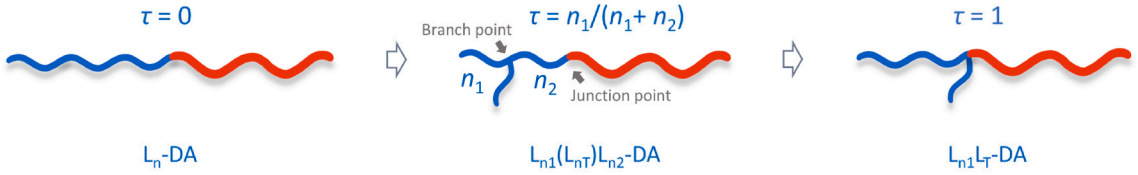
The resultant branched copolymers were verified by nuclear magnetic resonance spectroscopy (NMR), size exclusion chromatography (SEC), and matrix-assisted laser desorption/ionization time-of-flight mass spectrometry (MALDI-ToF MS) (Fig. 1 and S1-S4). Each sample gives a narrow, unimodal SEC elution trace that shifts to lower retention volume as successive block extension, corresponding to increased hydrodynamic volumes. MALDI-ToF MS exhibit a single peak where the observed molecular mass is in excellent agreement with the calculated value, confirming both the discrete feature and precise chemical structures. ^{1}H NMR spectra show the expected DA and L resonances with integrals quantitatively agree with the proposed structures (Fig. S1). Collectively, these characterizations confirm the successful synthesis of complex branched copolymers with precisely defined architecture and virtually free of other contaminants.

In this study, two sets of discrete block isomers were prepared, differing only in the branch-point location. Their MALDI-ToF MS spectra are superimposable (Fig. 2), and their SEC elution traces nearly overlap (Fig. S5), indicating that the sole difference among these isomers is their branching position. The linear block copolymers have a lower molecular weight than the branched counterparts due to the lack of the Y-shaped adaptor.

Microscopic phase separation is driven by the chemical immiscibility between the L and DA blocks. The morphologies can be regulated by varying volume fraction (f_A) and the branch position (τ). Benefiting from the low glass transition temperature and the absence of chain entanglement, these materials readily form ordered nanostructures after a brief thermal processing. Experimentally, the bulk samples were first heated to 130 °C for 10 min, followed by equilibration at 30 °C for 2 h. The resulting structures were characterized using small-angle X-ray scattering (SAXS).

Fig. 3 presents the SAXS profiles for two sets of isomeric branched block copolymers in which the minority L block is dispersed in the DA matrix. Each set shares an identical total L volume fraction but differ in the branch-point location, as quantified by the dimensionless parameter τ. For the L_{40}-DA_{32} series (Fig. 3a), the linear-linear block copolymer L_{40}-DA_{32} ($\tau = 0$) self-assembles into a Frank-Kasper σ phase (Fig. S12b), a complex tetragonal unit cell containing 30 distorted spheres (Fig. 3a, bottom). As τ increases, the architecture change drives a phase transition to hexagonally packed cylindrical (HEX) phases. This is confirmed by the q/q^* ratio of 1: $\sqrt{3}$: $\sqrt{7}$ in the SAXS profiles ($\tau = 0.25$ to 0.75; Fig. 3a). At $\tau = 1$, on the other hand, the branch point coincides with the A/B junction, and the copolymer transforms into an asymmetric linear-branched architecture. This structural shift triggers another phase transition to a BCC spherical phase, as confirmed by a characteristic q/q^* ratio of 1: $\sqrt{2}$: $\sqrt{3}$: $\sqrt{4}$ (Fig. 3a, top).

A transition from HEX to σ phase was recorded in the L_{40}-DA_{24} series with larger f_A (Fig. 3b). The linear diblock copolymer L_{40}-DA_{24} forms a



Scheme 1. Linear-Branched Block Copolymers with a Tunable Branch-point Location.

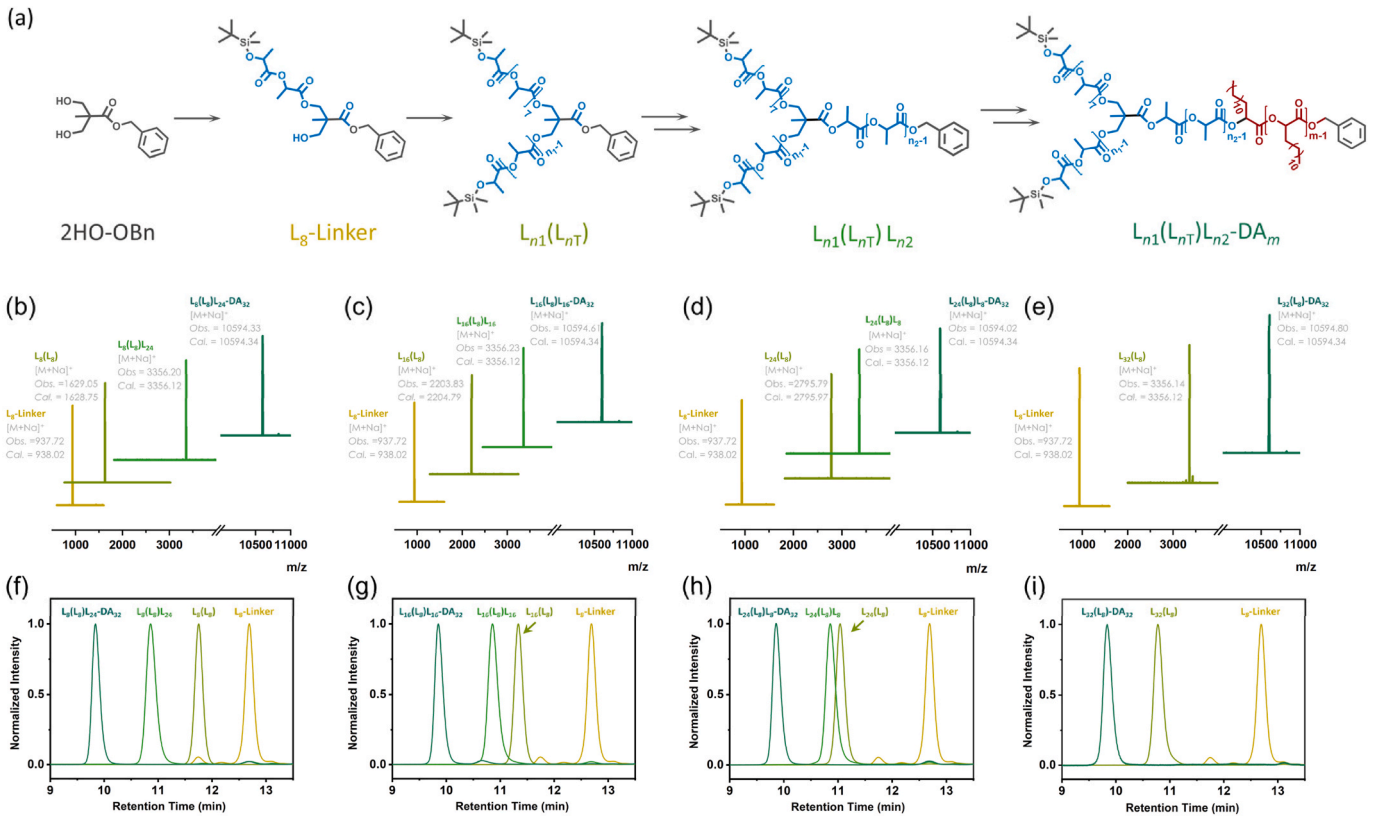


Fig. 1. (a) Synthetic route of the linear−branched block copolymers; (b-i) representative MALDI-ToF MS and SEC traces: L_8 (L_8)L_{24}-DA_{32} (b, f), L_{16} (L_8)L_{16}-DA_{32} (c, g), L_{24} (L_8)L_8-DA_{32} (d, h), and L_{32} (L_8)-DA_{32} (e, i).

Table 1
Molecular and structural characterization of discrete block copolymers.

Sample	MW_{cal}[a]	MW_{obs}[b]	f_A[c]	τ[d]	phase[e]	lattice dimension[f]	T_{ODT}[g]
L_{40}-DA_{24}	8531.65	8554.83	0.27	0	HEX	14.97	180
L_8 (L_8)L_{24}-DA_{24}	8761.79	8784.90	0.27	0.25	HEX	16.25	130
L_{16} (L_8)L_{16}-DA_{24}	8761.79	8784.38	0.27	0.5	HEX	16.39	150
L_{24} (L_8)L_8-DA_{24}	8761.79	8784.64	0.27	0.75	HEX	15.40	110
L_{32} (L_8)-DA_{24}	8761.79	8785.42	0.27	1	σ	$43.10^2 \times 22.66$	60
L_{40}-DA_{32}	10342.21	10365.42	0.22	0	σ	$39.39^2 \times 20.79$	>180
L_8 (L_8)L_{24}-DA_{32}	10571.35	10594.33	0.22	0.25	HEX	15.18	150
L_{16} (L_8)L_{16}-DA_{32}	10571.35	10594.61	0.22	0.5	HEX	14.52	170
L_{24} (L_8)L_8-DA_{32}	10571.35	10594.02	0.22	0.75	HEX	14.24	150
L_{32} (L_8)-DA_{32}	10571.35	10594.80	0.22	1	BCC	15.04	100

[a] Overall calculated molecular weight, Da.
[b] Molecular weight observed by MALDI-ToF MS, $[M + Na]^+$, Da.
[c] Volume fraction of *o*LA block.
[d] Architectural parameter, $\tau = n_1/(n_1+n_2)$.
[e] Phase, determined by SAXS.
[f] Lattice dimensions: intercolumn distances of HEX, or lattice parameters of σ and BCC phases, nm.
[g] Order-to-disorder transition temperature (°C), determined by SAXS. See Supporting Information for detailed calculations.

HEX morphology. As τ increases from 0 to 0.75 (corresponding to L_8 (L_8)L_{24}-DA_{24}, L_{16} (L_8)L_{16}-DA_{24}, and L_{24} (L_8)L_8-DA_{24}), the HEX phase remains. The domain spacing, however, follows a non-monotonic trend, increasing from 14.97 nm ($\tau = 0$) to 16.25 nm ($\tau = 0.25$), reaching a maximum of 16.39 nm ($\tau = 0.5$) and then decreasing slightly to 15.40 nm ($\tau = 0.75$). When τ reaches 1, the structure transitions to the Frank-Kasper σ phase (L_{32} (L_8)-DA_{24}; Fig. S12a), with lattice parameters determined as $a = b = 43.10$ nm, $c = 22.66$ nm, and an average polyhedral diameter $<D>$ of 13.88 nm. The underlying mechanism for this non-monotonic variation in domain spacing will be discussed in detail later.

In terms of thermal stability, a distinct difference exists between the linear copolymer ($\tau = 0$) and branched copolymers ($0 < \tau < 1$) in their order-disorder transition temperature (T_{ODT}). The linear-linear copolymer L_{40}-DA_{24} ($\tau = 0$) exhibits a T_{ODT} above 180 °C, while all branched copolymers show substantially lower T_{ODT} values (Table 1). This reduced thermal stability of branched copolymers originates from the increased number of chain ends introduced by the branching structure, which enhances entropy and thereby weakens the thermodynamic stability of the ordered phase.

To elucidate the influence of polymer architecture on phase evolution, we complied our experimental results into a phase portrait parameterized by f_A and τ (Fig. 4a). In general, phase transitions occur when τ approaches the extremes ($\tau \to 0$ and $\tau \to 1$), whereas a broad HEX

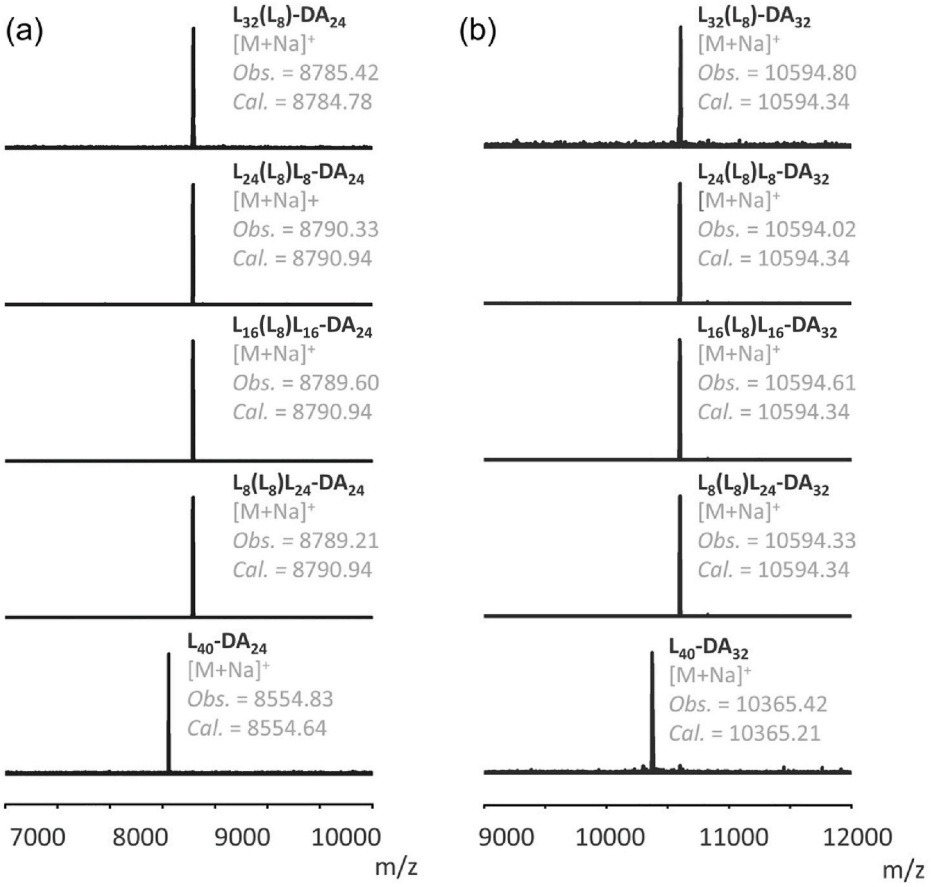


Fig. 2. MALDI-ToF MS of the discrete block copolymers with different architectures: L_{40}-DA_{24} series (a) and L_{40}-DA_{32} series (b).

region is observed for $0 < \tau < 1$, accompanied by non-monotonic variations in domain spacing. Interestingly, although molecular shape variations typically lead to monotonic structural shifts, the observed non-monotonic trend suggests the presence of multifactorial driving forces.

To understand the phase behaviors in the experiments, SCFT calculations were performed to construct the phase diagrams of the system. The $A_1A_TA_2$-B branched block copolymer melts are described by the "standard" model [35]. A description of the SCFT framework for the $A_1A_TA_2$-B block copolymer melts is provided in the Supporting Information. According to our previous work, the conformational asymmetry between the DA and L blocks (b_A/b_B) is approximately 1.84 [36]. Fig. 4b presents the SCFT phase diagram of $A_1A_TA_2$-B block copolymer melts in the f_A-τ plane at $\chi N = 25$ and $b_A/b_B = 1.84$, which is in qualitative agreement with experimental results. At $\tau = 0$, the $A_1A_TA_2$-B copolymer exhibits a Frank-Kasper σ phase window for $0.230 < f_A < 0.263$; this phase is stabilized by conformational asymmetry [37]. For $\tau < 0.74$, increasing τ expands the stable HEX phase region into the σ phase region, and this expansion is primarily attributed to reduced conformational asymmetry resulting from the branched A_T segment which counterbalances the difference between statistic segmental lengths. Further increasing τ induce a transition from HEX to spherical phase. When the A_T branch segment approaches the A/B interface, it constitutes a shell domain, while the longer A block extends inward to form the core domain. The synergies between the long and short blocks effectively relieves packing frustration, prompting the formation of spherical phase [6,22,38].

The domain spacing is determined within the SCFT framework by minimizing the free energy with respect to the unit-cell parameters. The SCFT predicts a monotonic variation of the domain spacing when all A-segment are treated as identical and assigned a uniform statistical segment length b_A (see Fig. S6b); consequently, the model fails to capture the experimentally observed non-monotonic dependence of the bulk periodicity on τ. To resolve this discrepancy, we modify the chain model by introducing a localized stiffening of the A-block: a fraction of A segments in the immediate vicinity of the branch point is assigned a larger statistical segment length than the remainder of the A block, reflecting enhanced local rigidity (see Fig. S6a). A detail description of the SCFT framework for the modified model is provided in the Supporting Information. With this modification, the SCFT predictions recover the non-monotonic variation in domain spacing (Fig. S6b), which is qualitatively consistent with the experimental measurements, confirming that local stiffening near the branch point can have a pronounced impact on the bulk periodicity.

Transition from linear ($\tau = 0$) to its linear-branched counterpart ($\tau > 0$) exerts a profound influence on the interfacial curvature. The self-assembly of block copolymer involves a hierarchical process: wedge- or cone-like copolymers assemble into discrete cylinderical or spherical motifs, which then further organize into ordered lattices [39]. Introducing *o*LA branch segment offsets the conformational asymmetry between the two blocks and, consequently, leads to a significant decrease in interfacial curvature. This point is corroborated by two observations: the variation in domain size of the HEX phase in the L-DA_{24} series, and the σ-to-HEX phase transition in the L-DA_{32} series; both phenomena are consistent with the same underlying mechanism (Scheme 2). The reduced interfacial curvature effectively flattens the shape of subunits, manifesting either as an increase in cylindrical domain size or as a morphological transition from spheres (3D cones) to HEX (2D wedges) [37,40].

A non-monotonic dependence on τ is observed also on the transition temperature (T_{ODT}). As shown in Fig. 5a, T_{ODT} first increases and then decreases as τ rises from 0.25 to 0.75, with a maximum near $\tau = 0.5$; representative data for the L_{40}-DA_{32} and L_{40}-DA_{24} series are provided in

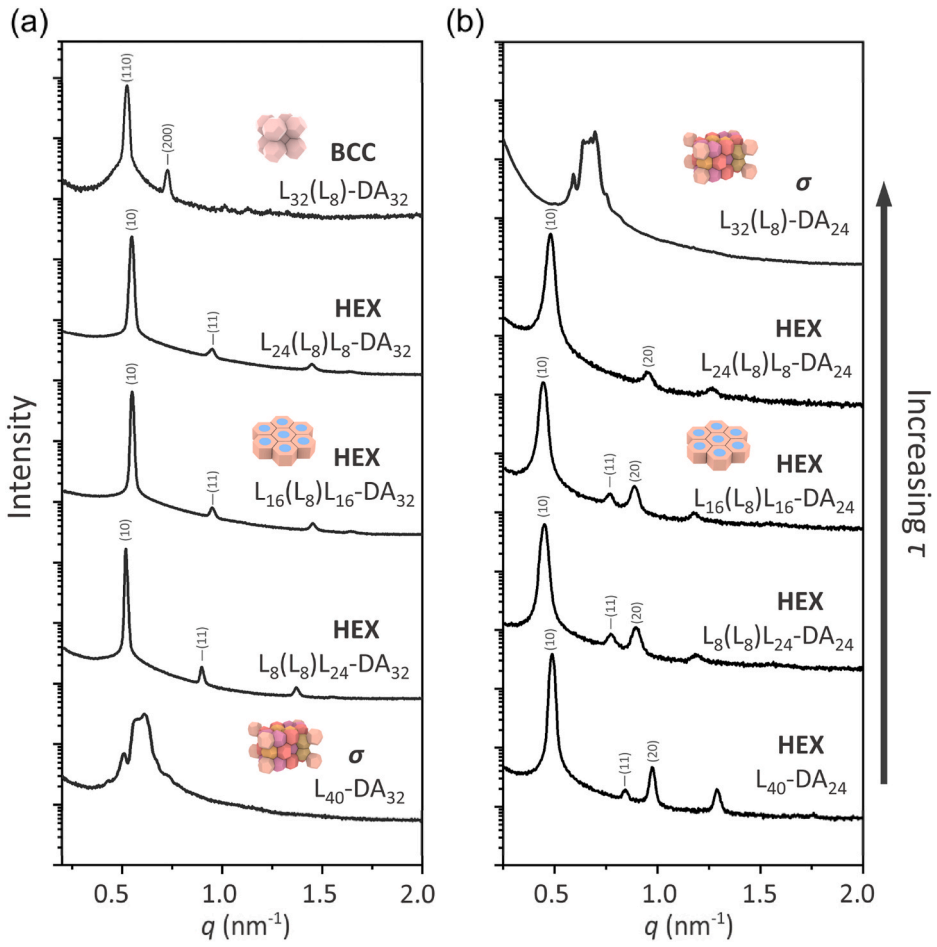


Fig. 3. SAXS profiles of block copolymers with varying architecture parameters: L_{40}-DA_{32} series (a) and L_{40}-DA_{24} series (b).

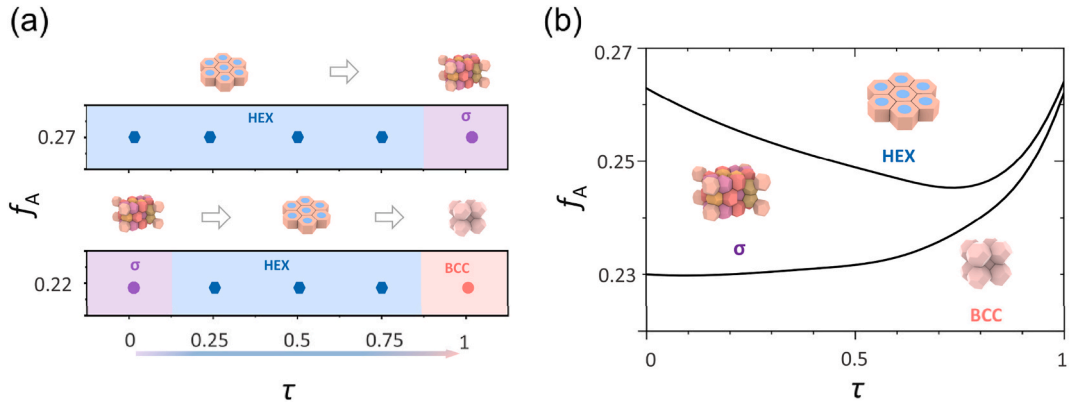
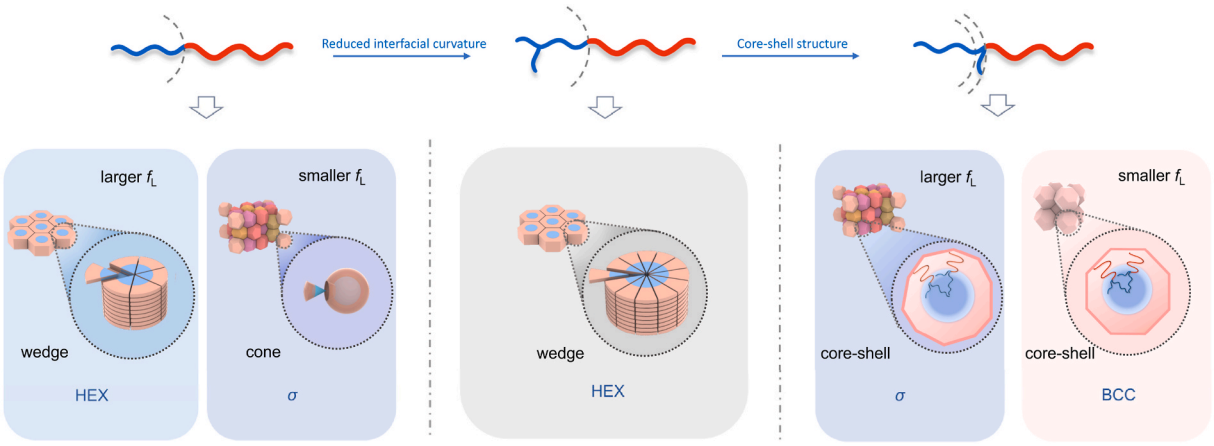


Fig. 4. (a) Phase portrait of block copolymers as a function of *o*LA volume fraction (f_A) and architectural parameter (τ). (b) SCFT phase diagram of $A_1A_TA_2$-B branched block copolymer melts in the f_A-τ plane at $\chi N = 25$ and $b_A/b_B = 1.84$.

SI (Fig. S7–8). To validate the universality of this trend, we performed SCFT calculation and constructed a phase diagram of $A_1A_TA_2B$ block copolymer melts in the χN-τ plane at $f_A = 0.25$ (Fig. 5b). The calculations reveal that, regardless of τ, decreasing χN drives the system through a transition sequence from initial HEX phase to σ and BCC phases before reaching the disordered phase. The phase boundaries among the neighboring phases show a non-monotonic trend. Given that the HEX phase near the χN_{ODT} is metastable in SCFT, we specifically calculated the boundary between this metastable HEX phase and the disordered phase, which is shown as the dashed line in Fig. 5b. While not in perfect agreement, χN_{ODT} still exhibits a non-monotonic dependence on τ, consistent with our experimental findings. The discrepancy between experimental and SCFT results near the ODT may be attributed to fluctuation effects as reported in previous studies [14,26,41].

To rationalize the HEX-to-sphere transition observed upon increasing τ from 0.75 to 1, we first examine how the branch-point location modifies the spatial distributions of A and B segments at fixed χN. We define $\Delta\phi_{max} = \phi_A(\mathbf{r}_m) - \phi_B(\mathbf{r}_m)$ for a given phase, where $\phi_A(\mathbf{r})$ and $\phi_B(\mathbf{r})$ are the volume fraction fields of A and B segments, respectively, and $\mathbf{r}_m$ denotes the spatial position at which the composition



Scheme 2. Schematic illustration of block copolymer self-assembly with increasing τ (from 0 to 1). Left: The branched architecture offsets the conformational disparity, thereby reducing interfacial curvature. Right: Cooperative interplay between the long and short chains induces a core–shell structure and stabilizes the Frank–Kasper phases.

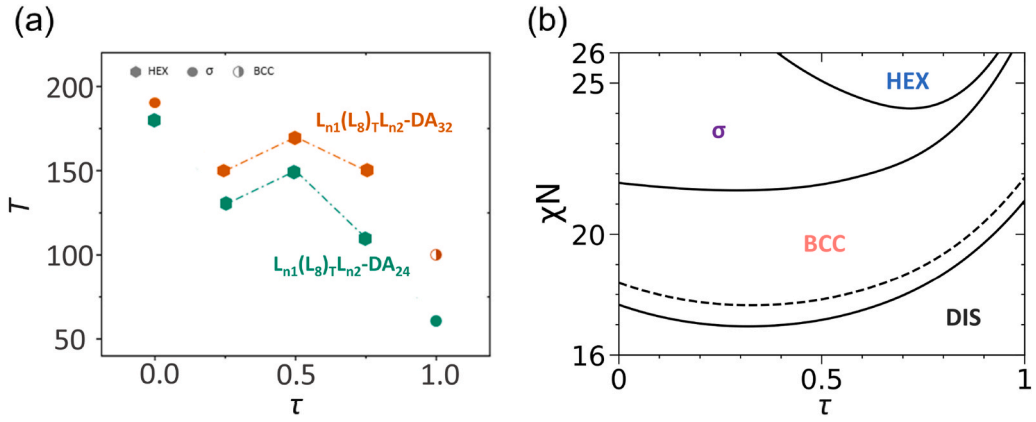


Fig. 5. (a) Variation of T_{ODT} with architectural parameter τ. (b) SCFT phase diagram of $A_1A_TA_2$-B branched block copolymer melts at $f_A = 0.25$. The dashed line represents the transition between the metastable HEX and disorder phases.

contrast $\phi_A(\mathbf{r}) - \phi_B(\mathbf{r})$ reaches its maximum. Thus, $\Delta\phi_{max}$ provides a measure of the strongest local segregation of A and B segments. As shown in Fig. 6a, $\Delta\phi_{max}$ remains nearly independent of τ up to $\tau \sim 0.75$ but decreases as τ approaches 1. This decrease is relatively modest for the BCC and σ phases but substantially larger for the HEX phase. Therefore, moving the branch point toward the A/B interface weakens the local A/B composition contrast, with the cylindrical HEX domains being particularly more sensitive to the architectural change than the spherical phases.

The spatial origin of this reduction is illustrated in Fig. 6b by the spatial variation in the A-segment volume fraction as τ increases from 0.75 to 1, *i.e.*, $\Delta\phi_A(\mathbf{r}) = \phi_{A,\tau=1}(\mathbf{r}) - \phi_{A,\tau=0.75}(\mathbf{r})$ for the σ phase. The redistribution of the A-segments is strongly nonuniform. It is evident that the A-segment volume fraction at the center of the A-rich domains

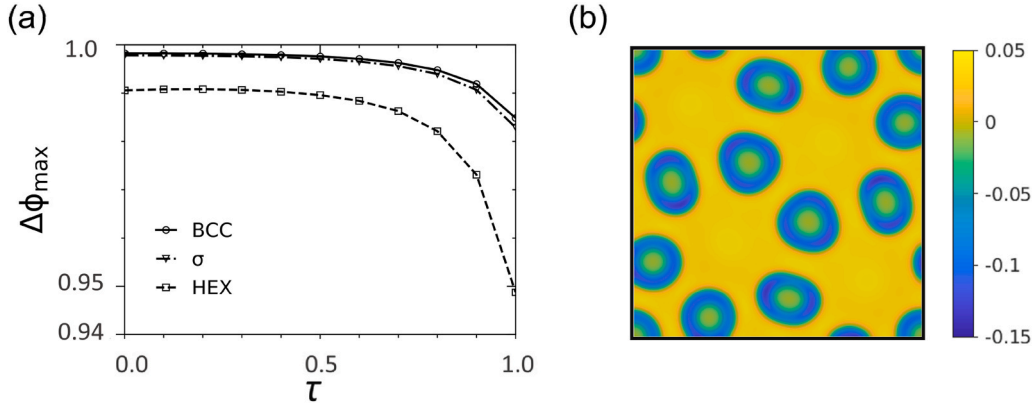


Fig. 6. (a) $\Delta\phi_{max}$ as a function of τ for BCC, HEX, and FK σ phases. (b) $\Delta\phi_A(\boldsymbol{r}) \equiv \phi_{A,\tau=1}(\boldsymbol{r}) - \phi_{A,\tau=0.75}(\boldsymbol{r})$ for σ phase [the (001) plane]. $f_A = 0.26$, $\chi N = 25$, and $b_A/b_B = 1.84$.

(the core regions) is slightly reduced, with $\Delta\phi_A(\mathbf{r}) \approx -0.006$ (Fig. 6b). In contrast, a pronounced depletion occurs in the intermediate region between the core and shell.

Figures S13-S15 further resolve this redistribution by decomposing the A-segment volume-fraction profiles into the contributions from the A_1, A_2, and A_T blocks for σ, HEX, and BCC phases at $\tau = 0.75$ and 1. In the former case, the A_1 and A_2 blocks predominantly occupy the inner regions of the A-rich domains, whereas the A_T block is preferentially enriched near the domain boundaries (the shell regions). At $\tau = 1$, the A_2 contribution is absent, the core is dominated by the A_1 block, and the A_T block remains localized near the shell region. Nevertheless, the maximum A_T volume fraction decreases from 0.161 to 0.117 for the FK σ phase, from 0.159 to 0.115 for the BCC phase, and from 0.149 to 0.114 for the HEX phase. At the same time, the maximum total A-segment volume-fraction decrease from 0.998 to 0.993, from 0.998 to 0.992, and from 0.992 to 0.974, for σ, BCC and HEX phases, respectively. The core and shell regions both become slightly less A-rich as shown in Fig. S13–S15.

This regulated core–shell structure provides a microscopic mechanism for the HEX-to-spheres transition. When the branch point approaches the A/B interface, the A_T branch segments preferentially reside near the outer part of the A domain (see Fig. S10–S12), but the overall A enrichment of this region is reduced. The redistribution of A-segments promotes greater interpenetration between A and B segments and weakens the effective segregation at fixed χN. The resulting diffuse interface can reduce the interfacial free-energy penalty associated with the more highly curved interfaces of the spherical domains. In contrast, the conformational and packing penalty associated with maintaining continuous cylindrical domains remains [42]. The free-energy balance can therefore make the spherical phases more favorable under weaken effective segregation strength, resulting in a HEX-to-sphere transition at τ close to 1.

3. Conclusions

In this work, we used a series of $A_1A_TA_2B$ block copolymers to systematically investigate the effect of branch-point location on the phase behavior of linear-branched block copolymers. As the branch-point location shifts from the free end of the A block toward the A/B interface, the system exhibits non-linear phase changes, transitioning from spherical phase to cylindrical phase and back to spherical phase. Compared with interfacial branching, intra-domain branching enhanced the segregation ability of block copolymers, and adjusting the branch-point position also altered the thermal stability of the system. This work underscores the critical role of topological design in directing self-assembly pathways and provides a strategic approach to accessing nonclassical nanostructures through precise architectural regulation.

CRediT authorship contribution statement

Tianyu Zheng: Writing – original draft, Investigation, Data curation. **Juntong He:** Writing – original draft, Investigation, Formal analysis. **Zhanhui Gan:** Investigation. **Jinbin Li:** Data curation. **Zhuang Ma:** Writing – review & editing, Data curation. **Jiajia Zhou:** Writing – review & editing, Formal analysis. **Xue-Hui Dong:** Writing – review & editing, Supervision, Funding acquisition, Conceptualization.

Notes

The authors declare no competing financial interest.

Declaration of competing interest

The authors declare that they have no known competing financial interests or personal relationships that could have appeared to influence the work reported in this paper.

Acknowledgments

This work was supported by National Natural Science Foundation of China (22273026, 22573034), Guangdong Basic and Applied Basic Research Foundation (2024A1515012401), and Fundamental Research Funds for the Cornell University (2025ZYGXZR003). We thank the staff of Beamline BL16B1 at the Shanghai Synchrotron Radiation Facility (SSRF) for assistance with the SAXS experiments.

Appendix A. Supplementary data

Supplementary data to this article can be found online at https://doi.org/10.1016/j.polymer.2026.130758.

Data availability

Data will be made available on request.

References

[1] Y. Mai, A. Eisenberg, Self-assembly of block copolymers, Chem. Soc. Rev. 41 (18) (2012) 5969–5985, https://doi.org/10.1039/C2CS35115C.
[2] F.S. Bates, Polymer-polymer phase behavior, Science 251 (4996) (1991) 898–905, https://doi.org/10.1126/science.251.4996.898.
[3] C.M. Bates, F.S. Bates, 50th anniversary perspective: Block Polymers—pure potential, Macromolecules 50 (1) (2017) 3–22, https://doi.org/10.1021/acs.macromol.6b02355.
[4] M.W. Matsen, F.S. Bates, Unifying weak-and strong-segregation block copolymer theories, Macromolecules 29 (4) (1996) 1091–1098, https://doi.org/10.1021/ma951138i.
[5] Z. Xu, Q. Dong, W. Li, Architectural design of block copolymers, Macromolecules 57 (5) (2024) 1869–1884, https://doi.org/10.1021/acs.macromol.3c01730.
[6] Y. Qiang, W. Li, A.-C. Shi, Stabilizing phases of block copolymers with gigantic spheres via designed chain architectures, ACS Macro Lett. 9 (5) (2020) 668–673, https://doi.org/10.1021/acsmacrolett.0c00193.
[7] M.W. Matsen, Effect of architecture on the phase behavior of AB-type block copolymer melts, Macromolecules 45 (4) (2012) 2161–2165, https://doi.org/10.1021/ma202782s.
[8] W. Jiang, Y. Qiang, W. Li, F. Qiu, A.-C. Shi, Effects of chain topology on the self-assembly of AB-type block copolymers, Macromolecules 51 (4) (2018) 1529–1538, https://doi.org/10.1021/acs.macromol.7b02389.
[9] Y. Zeng, S. Wang, Z. Xu, Z. Gan, X.-H. Dong, Discrete cyclic polymers with uniform chain length, Macromolecules 57 (19) (2024) 9379–9385, https://doi.org/10.1021/acs.macromol.4c01718.
[10] K.D. Dorfman, Frank–kasper phases in block polymers, Macromolecules 54 (22) (2021) 10251–10270, https://doi.org/10.1021/acs.macromol.1c01650.
[11] F.S. Bates, M.A. Hillmyer, T.P. Lodge, C.M. Bates, K.T. Delaney, G.H. Fredrickson, Multiblock polymers: Panacea or Pandora's box? Science 336 (6080) (2012) 434–440, https://doi.org/10.1126/science.1215368.
[12] J. Park, S. Jang, J. Kon Kim, Morphology and microphase separation of star copolymers, J. Polym. Sci., Part B: Polym. Phys. 53 (1) (2015) 1–21, https://doi.org/10.1002/polb.23604.
[13] G. Polymeropoulos, G. Zapsas, K. Ntetsikas, P. Bilalis, Y. Gnanou, N. Hadjichristidis, *50th anniversary perspective*: polymers with complex architectures, Macromolecules 50 (4) (2017) 1253–1290, https://doi.org/10.1021/acs.macromol.6b02569.
[14] G.M. Grason, B. DiDonna, R.D. Kamien, Geometric theory of diblock copolymer phases, Phys. Rev. Lett. 91 (5) (2003) 058304, https://doi.org/10.1103/PhysRevLett.91.058304.
[15] G.M. Grason, R.D. Kamien, Self-consistent field theory of multiply branched block copolymer melts, Phys. Rev. 71 (5) (2005) 051801, https://doi.org/10.1103/PhysRevE.71.051801.
[16] S.T. Milner, Chain architecture and asymmetry in copolymer microphases, Macromolecules 27 (8) (1994) 2333–2335, https://doi.org/10.1021/ma00086a057.
[17] M.W. Bates, S.M. Barbon, A.E. Levi, I.I.I.R.M. Lewis, H.K. Beech, K.M. Vonk, C. Zhang, G.H. Fredrickson, C.J. Hawker, C.M. Bates, Synthesis and self-assembly of AB n miktoarm star polymers, ACS Macro Lett. 9 (3) (2020) 396–403, https://doi.org/10.1021/acsmacrolett.0c00061.
[18] Y. Sun, R. Tan, Z. Ma, Z. Gan, G. Li, D. Zhou, Y. Shao, W.-B. Zhang, R. Zhang, X.-H. Dong, Discrete block copolymers with diverse architectures: resolving complex spherical phases with one monomer resolution, ACS Cent. Sci. 6 (8) (2020) 1386–1393, https://doi.org/10.1021/acscentsci.0c00798.
[19] N. Xie, W. Li, F. Qiu, A.-C. Shi, σ phase formed in conformationally asymmetric AB-type block copolymers, ACS Macro Lett. 3 (9) (2014) 906–910, https://doi.org/10.1021/mz500445v.
[20] Z. Ma, D. Zhou, M. Xu, Z. Gan, T. Zheng, S. Wang, R. Tan, X.-H. Dong, Discrete linear–branched block copolymer with broken architectural symmetry, Macromolecules 56 (3) (2023) 833–840, https://doi.org/10.1021/acs.macromol.2c02529.

[21] Z. Ma, Z. Liu, T. Zheng, Z. Gan, R. Tan, X.-H. Dong, Discrete miktoarm star block copolymers with tailored molecular architecture, ACS Polym. Au 3 (6) (2023) 457–465, https://doi.org/10.1021/acspolymersau.3c00017.
[22] J. Li, J. Xie, Z. Gan, S. Wang, X. Feng, A.-C. Shi, X.-H. Dong, Effect of molecular symmetry on the self-assembly behavior of AB2 linear–branched block copolymers, Macromolecules 57 (22) (2024) 10648–10656, https://doi.org/10.1021/acs.macromol.4c02230.
[23] W. Li, C. Duan, A.-C. Shi, Nonclassical spherical packing phases self-assembled from AB-Type block copolymers, ACS Macro Lett. 6 (11) (2017) 1257–1262, https://doi.org/10.1021/acsmacrolett.7b00756.
[24] F. Bates, R. Cohen, C. Berney, Small-angle neutron scattering determination of macrolattice structure in a polystyrene-polybutadiene diblock copolymer, Macromolecules 15 (2) (1982) 589–592, https://doi.org/10.1021/ma00230a073.
[25] Y. Sun, R. Tan, Z. Ma, D. Zhou, J. Li, D. Kong, X.-H. Dong, Quantify the contribution of chain length heterogeneity on block copolymer self-assembly, Giant 4 (2020) 100037, https://doi.org/10.1016/j.giant.2020.100037.
[26] M.W. Bates, J. Lequieu, S.M. Barbon, R.M. Lewis III, K.T. Delaney, A. Anastasaki, C. J. Hawker, G.H. Fredrickson, C.M. Bates, Stability of the A15 phase in diblock copolymer melts, Proc. Natl. Acad. Sci. 116 (27) (2019) 13194–13199, https://doi.org/10.1073/pnas.1900121116.
[27] G.E. Stein, Surprising states of order for linear diblock copolymers, Science 356 (6337) (2017) 487–488, https://doi.org/10.1126/science.aan1488.
[28] A.-C. Shi, Frustration in block copolymer assemblies, J. Phys. Condens. Matter 33 (25) (2021) 253001, https://doi.org/10.1088/1361-648X/abf8d0.
[29] S. Zhao, J. Yu, Z. Liu, J. Zhang, Y. Yan, Q. Dong, A.-C. Shi, X. Zhang, Phase behavior of linear-star topology-transformable block copolymers, Macromolecules 57 (8) (2024) 3831–3840, https://doi.org/10.1021/acs.macromol.3c02569.
[30] C. Li, Q. Dong, W. Li, Largely tunable asymmetry of phase diagrams of A (AB) n miktoarm star copolymer, Macromolecules 53 (24) (2020) 10907–10917, https://doi.org/10.1021/acs.macromol.0c02272.
[31] Q. Xie, Y. Qiang, L. Chen, Y. Xia, W. Li, Synergistic effect of stretched bridging block and released packing frustration leads to exotic nanostructures, ACS Macro Lett. 9 (7) (2020) 980–984, https://doi.org/10.1021/acsmacrolett.0c00313.
[32] R. Tan, D. Zhou, B. Liu, Y. Sun, X. Liu, Z. Ma, D. Kong, J. He, Z. Zhang, X.-H. Dong, Precise modulation of molecular weight distribution for structural engineering, Chem. Sci. 10 (46) (2019) 10698–10705, https://doi.org/10.1039/C9SC04736K.
[33] D. Cai, J. Li, Z. Ma, Z. Gan, Y. Shao, Q. Xing, R. Tan, X.-H. Dong, Effect of molecular architecture and symmetry on self-assembly: a quantitative revisit using discrete ABA triblock copolymers, ACS Macro Lett. 11 (4) (2022) 555–561, https://doi.org/10.1021/acsmacrolett.1c00788.
[34] S. Wang, Q. He, X.-T. Chen, D.-D. Zhou, Z.-H. Gan, X.-H. Dong, Discrete polyesters featuring a cyclic pendant group, Chin. J. Polym. Sci. (2026) 1–7, https://doi.org/10.1007/s10118-025-3502-8.
[35] G. Fredrickson, The Equilibrium Theory of Inhomogeneous Polymers, OUP Oxford, 2006.
[36] Z. Gan, Z. Xu, K. Tian, D. Zhou, L. Li, Z. Ma, R. Tan, W. Li, X.-H. Dong, Stabilizing hexagonally close-packed phase in single-component block copolymers through rational symmetry breaking, Nat. Commun. 15 (1) (2024) 6581, https://doi.org/10.1038/s41467-024-50906-9.
[37] D. Zhou, M. Xu, Z. Ma, Z. Gan, J. Zheng, R. Tan, X.-H. Dong, Discrete diblock copolymers with tailored conformational asymmetry: a precise model platform to explore complex spherical phases, Macromolecules 55 (16) (2022) 7013–7022, https://doi.org/10.1021/acs.macromol.2c01202.
[38] G.K. Cheong, F.S. Bates, K.D. Dorfman, Symmetry breaking in particle-forming diblock polymer/homopolymer blends, Proc. Natl. Acad. Sci. 117 (29) (2020) 16764–16769, https://doi.org/10.1073/pnas.2006079117.
[39] D. Zhou, M. Xu, Z. Ma, Z. Gan, R. Tan, S. Wang, Z. Zhang, X.-H. Dong, Precisely encoding geometric features into discrete linear polymer chains for robust structural engineering, J. Am. Chem. Soc. 143 (44) (2021) 18744–18754, https://doi.org/10.1021/jacs.1c09575.
[40] E.E. Dormidontova, T.P. Lodge, The order− disorder transition and the disordered micelle regime in sphere-forming block copolymer melts, Macromolecules 34 (26) (2001) 9143–9155, https://doi.org/10.1021/ma010098h.
[41] T. Beardsley, M. Matsen, Fluctuation correction for the order–disorder transition of diblock copolymer melts, J. Chem. Phys. 154 (12) (2021), https://doi.org/10.1063/5.0046167.
[42] M.W. Matsen, The standard Gaussian model for block copolymer melts, J. Phys. Condens. Matter 14 (2) (2002) R21–R47, https://doi.org/10.1088/0953-8984/14/2/201.

Supporting Information

Phase Behaviors of Linear-Branched Block Copolymers with Precisely Tunable Branch-Point Locations

Tianyu Zheng,[1] Juntong He,[1] Zhanhui Gan,[1] Jinbin Li[1], Zhuang Ma,[2*] Jiajia Zhou,[1,3*] and Xue-Hui Dong[1,3*]

[1]South China Advanced Institute for Soft Matter Science and Technology, School of Emergent Soft Matter, South China University of Technology, Guangzhou 510640, China

[2]Institute of Materials Intelligent Technology, Liaoning Academy of Materials, Shenyang 110004, China

[3]Guangdong Provincial Key Laboratory of Functional and Intelligent Hybrid Materials and Devices, South China University of Technology, Guangzhou 510640, China

*Corresponding author: xdong@scut.edu.cn; zhouj2@scut.edu; zma@lam.ln.cn

1. Materials.

The following chemicals were used as received: meso-lactide (TCL, 85%), potassium carbonate (K_2CO_3, Greagent, 99%), ethyl acetate (EA, Greagent, > 99.5%), petroleum ether(PE, boiling range from 60 to 90 ℃, Greagent), diethyl acetamidomalonate (adamas, 98%), 1-bromododecane (adamas, 99%), cesium carbonate (Cs_2CO_3, adamas, 99.9%, 20 mesh), potassium iodide (KI, adamas, 99%), acetonitrile (CH_3CN, adamas, 99.9%), sodium hydroxide (NaOH, Greagent, 98%), ethanol (EtOH, adamas, 99.5%), sulfuric acid (H_2SO_4, adamas, 96%), acetic acid glacial (CH_3COOH, Sigma-Aldrich, 99%), tert-butyl nitrite (TCI, 90%), 1,4-dioxane (TCI, 98%), benzyl bromide (BnBr, TCI, 99%), tert-butyldimethylsilyl chloride (TBDMSCl, TCI, 98%), imidazole (TCI, 98%), Pd/C (Aldrich, 10 wt%), boron trifluoride etherate (BF_3-Et_2O, TCI, 98%), N,N'-diisopropylcarbodiimide (DIC, Aldrich, 99%), 4-(Dimethylamino)-pyridinium-4-toluenesulfonate (DPTS) was synthesized according to the literature. Other anhydrous solvents, including dichloromethane (CH_2Cl_2), toluene, were obtained with an INERT Pure Solv System (Inert Corporation, USA). The linker (2,2-bis(hydroxymethyl)propanoic acid benzyl ester) were prepared from 2,2-bis(hydroxymethyl)propanoicacid following the same procedure as described in our earlier study.

2. Characterizations.

Nuclear Magnetic Resonance (NMR). All ^1H NMR spectra were acquired in $CDCl_3$ using a Bruker 500 MHz NMR spectrometer. The spectra were referenced to the residual solvent peak of $CDCl_3$ at δ 7.26 ppm.

Size exclusion chromatography (SEC). SEC analyses were measured at 40 ℃ on a Tosoh HLC-8320 instrument equipped with three TSK gel columns (SuperH2000, SuperH3000, and SuperH4000 in series), a double-flow type RI detector, and a UV-8320 UV detector, using THF as eluent. The flow rate was 0.6 mL/min. Data acquisition was performed using EcoSEC software, and molecular weights and molecular weight distributions were calibrated with polystyrene standards (Polymer Laboratories).

Matrix-assisted laser desorption/ionization time-of-flight (MALDI-ToF). MALDI-ToF mass spectra of the samples were obtained on a Bruker Ultraflex III TOF/ToF mass spectrometer (Bruker Daltonics, Billerica, MA), equipped with a Nd:YAG laser emitting at a wavelength of 355 nm. All spectra were measured under positive linear mode. The mass scale was calibrated with standards of polystyrene. Trans-2-[3-(4-tertbutylphenyl)-2-methyl-2-propenyli-dene]-malononitrile (DCTB, Aldrich, >98%) served as

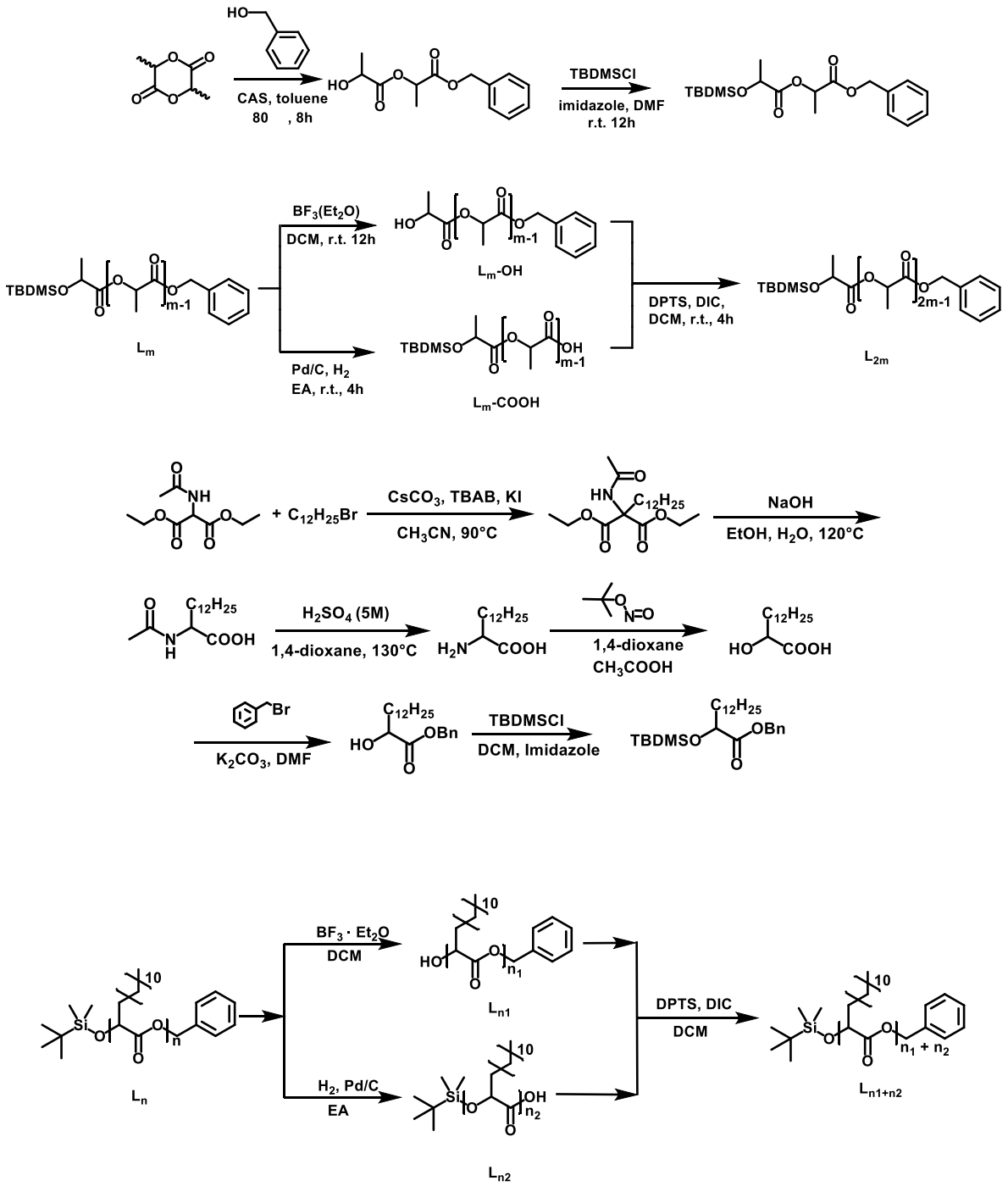
the matrix and trifluoroacetate (NaTFA) was used as the cationizing agent (10 mg/mL in methanol). The matrix and cationizing agent solutions were mixed in the ratio of 10/1 (*v*/*v*). In sample preparation, 0.5 μL of the matrix/salt mixture was deposited on microtiter plate wells (MTP 384-well ground steel plate). After allowing the spots to dry, 0.5 μL of sample solution (*ca.* 10 mg/mL in THF) was deposited on the top of the dry matrix/salt spot and adding another 0.5 μL of the matrix/salt mixture. After evaporation of the solvent, the target plate was loaded for data collection. Bruker's flex Analysis software was applied to analyze data.

Small angle X-ray scattering (SAXS). SAXS data were collected on Shanghai Synchrotron Radiation (SSRF), beamline BL16B1. The incident X-ray photon energy was 10 keV; the wavelength of the X-ray was 0.124 nm; the photo flux was 1×10^{11} phs/s; The beam size is around 0.4×0.5 mm^2. Scattered X-rays were captured on a two-dimensional Pilatus detector. The instrument was calibrated with diffraction patterns from silver behenate. Different annealing protocols have been applied. In general, samples were heated to above the order-to-disorder transition temperature (80 °C) for 10 minutes on a Linkam hot stage, and then annealed at 25 °C for 6 hours to facilitate ordered structure. *In-situ* experiments were carried out with a Linkam hot stage mounted onto the SAXS apparatus in BL16B1.Samples were sealed with aluminum foil for good thermal conductivity. The heating rate was 10 °C/min. Samples were equilibrated for 3 minutes at each temperature before collecting data.

3. Synthesis procedures

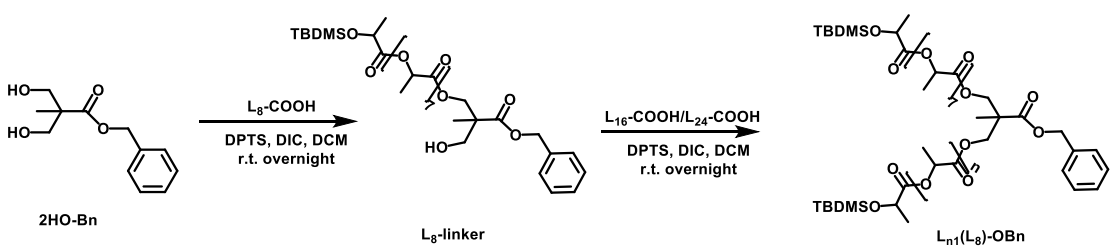
3.1 Synthesis of discrete *o*LA and *o*DA.

The synthesis of the *o*LA and *o*DA monomers can be found in our previous literature.



Scheme S1. Synthetic route of discrete *o*LA and *o*DA.

3.2 Synthesis of $L_{n1}(L_8)_T$-OBn



Scheme S2. Synthetic route of LA block $L_{n1}L_8$.

L_8-COOH: L_8 (2.00 g, 2.5 mmol) was dissolved in ethyl acetate (100 mL) and Pd/C (10 wt% on carbon, 0.16 g, 0.15 mmol, 5 eq) was added to the solution. The mixture was stirred for 12 hours under a hydrogen atmosphere. After that, TLC analysis (PE/EA, v/v, 60/40) confirmed that all the benzyl ester was converted. The black suspension was filtered through celite and the filter cake was washed with EA (50 mL × 3). The combined filtrates were concentrated in vacuo, giving L_8-COOH in high purity (1.92s g, 96%).

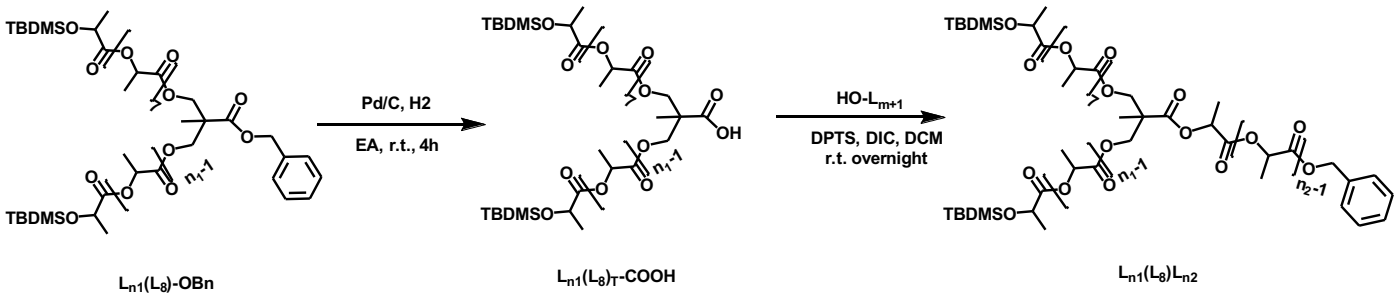
L_8-Linker: The linker (0.19mg, 0.81 mmol) and L_8-COOH (0.85 g, 10.62 mmol) were mixed in a 100 mL round-bottom flask. Anhydrous DCM (2 mL) and DPTS (20 mg, 0.07 mmol) were added under a nitrogen atmosphere. After dissolving completely, the solution was cooled to 0 ℃ by ice water. DIC (100 mg, 0.80 mmol) was added dropwise over 10 minutes. The solution was stirred for another 4 hours at room temperature. After that, the reaction mixture was washed with deionized water (100 mL) and extracted with DCM (50 mL × 3). The combined organic layers were dried over $MgSO_4$. The solvent was removed in vacuo and the crude product was purified by automated column chromatography with PE/EA (v/v, 60/40), giving pure product as a colorless solid (0.60 g, 70%). 1H NMR (500 MHz, $CDCl_3$, ppm, δ): 7.37-7.29 (5H, Ar-H), 5.28-5.00 (9H, Ar-CH_2O, $OCH(CH_3)CO$), 4.42-4.19 (5H, $-C(CH_3)(CH_2O-)_2$, $(CH_3)_3Si(CH_3)_2OCH(CH_3)CO$), 1.60-1.48 (21H, $-C(CH_3)CO$), 1.33-1.19 (3H, $-C(CH_3)(CH_2O-)_2$), 1.45-1.38 (3H, $(CH_3)_3Si(CH_3)_2OCH(CH_3)CO$); 0.90 (9H, $Si(CH_3)_2(CH_3)_3$); 0.13-0.06 (6H, $Si(CH_3)_2(CH_3)_3$). MS (MALDI-ToF): $[M+Na]^+$ Cal 938.02; Obs 937.72.

L_{n1}-COOH: Take L_{16} as an example. L_{16} (0.30 g, 0.21 mmol) was dissolved in ethyl acetate (100 mL) and Pd/C (10 wt% on carbon, 0.16 g, 0.15 mmol, 5 eq) was added into the solution. The mixture was stirred for 4 hours under a hydrogen atmosphere. After that, TLC analysis (PE/EA, v/v, 60/40) confirmed that all the benzyl ester was converted. The black suspension was filtered through celite and the filter cake was washed with EA (50 mL × 3). The combined filtrates were concentrated in vacuo, giving L_8-COOH in high purity (0.29 g, 96%).

L_{n1}(L_8)-OBn: Take $L_{16}(L_8)_T$-OBn as an example. The HO-$(L_8)_T$-OBn (0.15 g, 0.15 mmol) and L_{16}-COOH (0.29 g, 0.20 mmol) were mixed in a 25 mL round-bottom flask. Anhydrous DCM (2 mL) and DPTS (20 mg, 0.07 mmol) were added under a nitrogen atmosphere. After dissolving completely, the solution was cooled to 0 ℃ by ice water. DIC (100 mg, 0.80 mmol) was added dropwise over 10 minutes. The solution was stirred for another 12 hours at room temperature. After that, the reaction mixture was washed with deionized water (100 mL) and extracted with DCM (50 mL × 3). The combined organic layers were dried over $MgSO_4$. The solvent was removed in vacuo and the crude product was purified by automated column chromatography with PE/EA (v/v, 60/40), giving pure product as a colorless solid (0.35 g, 78%). 1H NMR (500 MHz, $CDCl_3$, ppm, δ): 7.37-7.29 (5H, Ar-H), 5.28-5.00 (26H, Ar-CH_2O, $OCH(CH_3)CO$), 4.42-4.19 (6H, $-C(CH_3)(CH_2O-)_2$, $(CH_3)_3Si(CH_3)_2OCH(CH_3)CO$), 1.60-1.48 (66H, $-C(CH_3)CO$), 1.33-1.19 (3H, $-C(CH_3)(CH_2O-)_2$), 1.45-1.38

(6H, $(CH_3)_3Si(CH_3)_2OCH(C\underline{H}_3)CO$); 0.90 (18H, $Si(CH_3)_2(C\underline{H}_3)_3$); 0.13-0.06 (12H, $Si(C\underline{H}_3)_2(CH_3)_3$). MS (MALDI-ToF): $[M+Na]^+$ Cal 1628.75; Obs 1629.05.

3.3 Synthesis of $L_{n1}(L_8)L_{n2}$



Scheme S2. Synthetic route of LA block $L_{n1}(L_8)L_{n2}$.

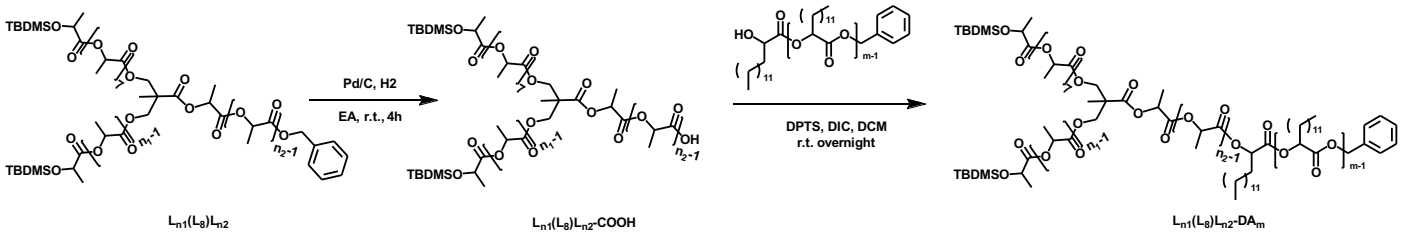
HO-L_{n2}: Take HO-L_{16} as an example. L_{16} (0.40 g, 0.29 mmol) was dissolved in DCM (4 mL) and the solution was cooled to 0 ℃ by ice water. BF_3-Et_2O (0.21 g, 1.45 mmol) was added dropwise over 10 minutes. Two hours later, sodium bicarbonate aqueous solution (30 mL) and brine (50 mL) was added slowly into the solution to quench the reaction. The organic phase was collected and the aqueous phase was extracted with EA (100 mL × 3). The combined organic layers were dried over Na_2SO_4. The crude product was purified by automated column chromatography with PE/EA (v/v, 60/40), giving the pure product as a colorless oil.

$L_{n1}(L_8)$-COOH: Take $L_{16}(L_8)_T$-COOHas an example. $L_{16}(L_8)_T$-COOH (0.35 g, 0.21 mmol) was dissolved in ethyl acetate (100 mL) and Pd/C (10 wt% on carbon, 0.16 g, 0.15 mmol, 5 eq) was added into the solution. The mixture was stirred for 4 hours under a hydrogen atmosphere. After that, TLC analysis (PE/EA, v/v, 60/40) confirmed that all the benzyl ester was converted. The black suspension was filtered through celite and the filter cake washed with EA (50 mL × 3). The combined filtrates were concentrated in vacuo, giving L_8-COOH in high purity (0.34 g, 98%).

$L_{n1}(L_8)L_{n2}$: Take $L_{16}(L_8)_TL_{16}$ as an example. The $L_{16}(L_8)_T$-COOH(0.35g, 0.17 mmol) and HO-L_{16} (0.20 g, 0.16 mmol) were mixed in a 25 mL round-bottom flask. Anhydrous DCM (1 mL) and DPTS (20 mg, 0.07 mmol) were added under a nitrogen atmosphere. After dissolving completely, the solution was cooled to 0 ℃ by ice water. DIC (100 mg, 0.80 mmol) was added dropwise over 10 minutes. The solution was stirred for another 12 hours at room temperature. After that, the reaction mixture was washed with deionized water (100 mL) and extracted with DCM (50 mL × 3). The combined organic layers were dried over $MgSO_4$. The solvent was removed in vacuo and the crude product was purified by automated column chromatography with PE/EA (v/v, 40/60), giving pure product as a colorless solid (0.30 g, 55%). 1H NMR (500 MHz, CDCl3, ppm, δ): 7.37-7.29 (5H, Ar-$\underline{H}$), 5.28-5.00 (40H, Ar-C$\underline{H}_2$O, OC$\underline{H}$(CH_3)CO), 4.42-4.19 (6H, -C(CH_3)(C$\underline{H}_2$O-)$_2$, $(CH_3)_3Si(CH_3)_2OC\underline{H}(CH_3)CO$), 1.60-1.48 (114H, -C(C$\underline{H}_3$)CO), 1.33-1.19 (3H, -C(C$\underline{H}_3$)(CH_2O-)$_2$), 1.45-1.38

(6H, $(CH_3)_3Si(CH_3)_2OCH(C\underline{H}_3)CO$); 0.90 (18H, $Si(CH_3)_2(C\underline{H}_3)_3$); 0.13-0.06 (12H, $Si(C\underline{H}_3)_2(CH_3)_3$). MS (MALDI-ToF): [M+Na]+ Cal 3356.12; Obs 3356.91.

3.4 Synthesis of $L_{n1}(L_8)L_{n2}$-DA_m



Scheme S3. Synthetic route of $L_{n1}(L_8)L_{n2}$-DA_m.

HO-DA_m: Take HO-DA_{32} as an example. DA_{32} (0.40 g, 0.05 mmol) was dissolved in DCM (1 mL) and the solution was cooled to 0 ℃ by ice water. BF_3-Et_2O (0.04 g, 0.28 mmol) was added dropwise over 10 minutes. Two hours later, sodium bicarbonate aqueous solution (6 mL) and brine (10 mL) was added slowly into the solution to quench the reaction. The organic phase was collected and the aqueous phase was extracted with EA (10 mL × 3). The combined organic layers were dried over Na_2SO_4. The crude product was purified by automated column chromatography with PE/EA (v/v, 95/05), giving the pure product as a colorless oil.

$L_{n1}(L_8)L_{n2}$-COOH: Take $L_{16}(L_8)_TL_{16}$COOH as an example. $L_{16}(L_8)_TL_{16}$-OBn (0.1 g, 0.03 mmol) was dissolved in ethyl acetate (20 mL) and Pd/C (10 wt% on carbon, 0.10 g, 0.10 mmol, 5 eq) was added into the solution. The mixture was stirred for 4 hours under a hydrogen atmosphere. After that, TLC analysis (PE/EA, v/v, 50/50) confirmed that all the benzyl ester was converted. The black suspension was filtered through celite and the filter cake washed with EA (20 mL × 3). The combined filtrates were concentrated in vacuo, giving HOOC-$L_{16}(L_8)_TL_{16}$ in high purity (0.09 g, 95%).

$L_{n1}(L_8)L_{n2}$-DA_m: Take $L_{16}(L_8)_TL_{16}$-DA_{32} as an example. The $L_{16}(L_8)_T$-COOH (0.09 g 0.17 mmol) and HO-DA_{32} (0.20 g, 0.03 mmol) were mixed in a 25 mL round-bottom flask. Anhydrous DCM (1 mL) and DPTS (20 mg, 0.07 mmol) were added under a nitrogen atmosphere. After dissolving completely, the solution was cooled to 0 ℃ by ice water. DIC (100 mg, 0.80 mmol) was added dropwise over 10 minutes. The solution was stirred for another 12 hours at room temperature. After that, the reaction mixture was washed with deionized water (100 mL) and extracted with DCM (50 mL × 3). The combined organic layers were dried over $MgSO_4$. The solvent was removed in vacuo and the crude product was purified by automated column chromatography with PE/EA (*v*/*v*, 40/60), giving pure product as a colorless solid (0.10 g, 33%). 1H NMR (500 MHz, $CDCl_3$, ppm, δ): 7.37-7.29 (5H, Ar-$\underline{H}$), 5.28-5.00 (72H, Ar-C$\underline{H}_2$O, OC$\underline{H}(CH_3)$CO and -OC$\underline{H}(CH_2)$CO-), 4.42-4.19 (6H, -C$(CH_3)(C\underline{H}_2O\text{-})_2$, $(CH_3)_3Si(CH_3)_2OC\underline{H}(CH_3)CO$), 2.04-1.82 (64H, -OCH(C$\underline{H}$2)CO-), 1.60-1.48 (114H, -C$(C\underline{H}_3)(CH_2O\text{-})_2$), 1.45-1.38 (6H, $(CH_3)_3Si(CH_3)_2OCH(C\underline{H}_3)CO$), 1.33-1.13 (643H, C$(C\underline{H}_3)(CH_2O\text{-})_2$,

$OCH_2CH_2(C\underline{H}_2)_9CH_3$); 0.90 (18H, CH2CH2CH3 and $Si(CH_3)_2(C\underline{H}_3)_3$); 0.13-0.06 (12H, $Si(C\underline{H}_3)_2(CH_3)_3$). MS (MALDI-ToF): $[M+Na]^+$ Cal 10559.32; Obs 10598.76.

4. Details on the Numerical Calculations of Self-Consistent Field Theory

We consider a model system for incompressible $A_1A_TA_2$-B branched block copolymer melts consisting of m chains, in volume V at thermodynamic temperature T. Each chain contains $N \equiv N_{A_1} + N_{A_T} + N_{A_2} + N_B$ segments in total, where N_{A_T} is the number of segments on the branched A-block, N_{A_1} is the number of segments on the A_1-block with one end connected to the branched site, N_{A_2} is the number of segments on the A_2-block with one end connected to the branched site and the other end connected to B-block, and N_B is the number of segments on the B-block. The location of the branched A-block is described by an architectural parameter $\tau \equiv N_{A_1}/(N_{A_1} + N_{A_2})$. Assuming that all segments have equal number density ρ_0, the volume fraction of the segment A in the copolymer is $f_A = f_{A_1} + f_{A_2} + f_{A_T}$ with $f_{A_1} \equiv N_{A_1}/N$, $f_{A_2} \equiv N_{A_2}/N$ and $f_{A_T} \equiv N_{A_T}/N$, and the volume fractions of the segment B is $f_B = 1 - f_A$. The chain connectivity is described by the continuous Gaussian chain model with a statistical segment length b_a for the segment of type α (=A, B). The chain connectivity is described by continuous Gaussian chain. For the non-bonded interactions, an A segment repels a B segment via the pair potential of $\delta(r)\chi/\rho_0$ with $\delta(r)$ being the Dirac-δ function and the Flory-Huggins parameter $\chi \geq 0$ controlling their repulsion strength.

The dimensionless Helmholtz free energy per chain can be expressed as

$$\beta f_c = \frac{1}{V}\left[\chi N \int d\mathbf{r} \phi_A(\mathbf{r})\phi_B(\mathbf{r}) - \int d\mathbf{r} \omega_A(\mathbf{r})\phi_A(\mathbf{r}) - \int d\mathbf{r} \omega_B(\mathbf{r})\phi_B(\mathbf{r}) \right] - \ln Q_c, \quad \text{(S1)}$$

where $\phi_\alpha(\mathbf{r})$ and $\omega_\alpha(\mathbf{r})$ are the volume fraction field and its conjugate potential field for the segments of type $\alpha = A,B$, respectively, and Q_c is the single chain partition function obtained by $Q_c = \frac{1}{V}\int d\mathbf{r} q_{p,q}(\mathbf{r},s) q_{q,p}(\mathbf{r},1-s)$. Here $q_{p,q}(\mathbf{r},s)$ is the propagator satisfying the modified diffusion equations (MDEs)

$$\frac{\partial q_{p,q}}{\partial s}(\mathbf{r},s) = \frac{b_\alpha^2}{b_B^2}\nabla^2 q_{p,q}(\mathbf{r},s) - \omega_\alpha(\mathbf{r}) q_{p,q}(\mathbf{r},s), \quad \text{(S2)}$$

starting from the vertex p and ending at the vertex q, where $0 \leq s \leq 1$ is the normalized chain contour variable along the block with vertices p and q being its two ends and the segment type α depends on vertices p and

q. The following lists the propagators for the blocks on a $A_1A_TA_2$-B branched block copolymer chain and their initial conditions:

Propagator	block	α	Initial Condition
$q_{0,1}(\mathbf{r},s)$	A_1	A	$q_{0,1}(\mathbf{r},s=0)=1$
$q_{2,1}(\mathbf{r},s)$	A_T	A	$q_{2,1}(\mathbf{r},s=0)=1$
$q_{4,3}(\mathbf{r},s)$	B	B	$q_{4,3}(\mathbf{r},s=0)=1$
$q_{3,1}(\mathbf{r},s)$	A_2	A	$q_{3,1}(\mathbf{r},s=0)=q_{3,4}(\mathbf{r},s=1)$
$q_{1,0}(\mathbf{r},s)$	A_1	A	$q_{1,0}(\mathbf{r},s=0)=q_{3,1}(\mathbf{r},s=1)q_{0,1}(\mathbf{r},s=1)$
$q_{1,3}(\mathbf{r},s)$	A_2	A	$q_{1,3}(\mathbf{r},s=0)=q_{0,1}(\mathbf{r},s=1)q_{2,1}(\mathbf{r},s=1)$
$q_{1,2}(\mathbf{r},s)$	A_T	A	$q_{1,2}(\mathbf{r},s=0)=q_{0,1}(\mathbf{r},s=1)q_{3,1}(\mathbf{r},s=1)$
$q_{3,4}(\mathbf{r},s)$	B	B	$q_{3,4}(\mathbf{r},s=0)=q_{1,3}(\mathbf{r},s=1)$

Under the mean-field approximation, we have the following self-consistent field (SCF) equations

$$\begin{cases} \omega_{\mathrm{A}} = \chi N\phi_{\mathrm{B}}(\mathbf{r})+\eta(\mathbf{r}) \\ \omega_{\mathrm{B}} = \chi N\phi_{\mathrm{A}}(\mathbf{r})+\eta(\mathbf{r}) \\ \phi_{\mathrm{A}}(\mathbf{r}) = \int_0^1 \mathrm{d}s q_{0,1}(\mathbf{r},s)q_{1,0}(\mathbf{r},N-s) \\ \qquad +\int_0^1 \mathrm{d}s q_{1,2}(\mathbf{r},s)q_{2,1}(\mathbf{r},N-s)\cdot \\ \qquad +\int_0^1 \mathrm{d}s q_{1,3}(\mathbf{r},s)q_{3,1}(\mathbf{r},N-s) \\ \phi_{\mathrm{B}}(\mathbf{r}) = \int_0^1 \mathrm{d}s q_{3,4}(\mathbf{r},s)q_{4,3}(\mathbf{r},N-s) \end{cases} \tag{S3}$$

Obviously, the volume-fraction fields of the A-segment can be decomposed into three parts $\phi_{\mathrm{A}}(\mathbf{r})=\phi_{\mathrm{A_1}}(\mathbf{r})+\phi_{\mathrm{A_T}}(\mathbf{r})+\phi_{\mathrm{A_2}}(\mathbf{r})$ (see Figure S9-S11), where $\phi_{\mathrm{A_1}}(\mathbf{r})=\int_0^1 \mathrm{d}s q_{0,1}(\mathbf{r},s)q_{1,0}(\mathbf{r},N-s)$,

$\phi_{\mathrm{A_T}}(\mathbf{r}) = \int_0^1 \mathrm{d}s q_{1,2}(\mathbf{r},s) q_{2,1}(\mathbf{r},N-s)$, and $\phi_{\mathrm{A_2}}(\mathbf{r}) = \int_0^1 \mathrm{d}s q_{1,3}(\mathbf{r},s) q_{3,1}(\mathbf{r},N-s)$.

Note that all A-segments have the same statistical segment length $b_{\mathrm{A}}/b_{\mathrm{B}} = 1.84$ in the above system (denoted model I). To introduce a local stiffening in the immediate vicinity of the grafting point, we modified the chain model as demonstrated in Figure S6a. Each chain now still contains $N = N_{\mathrm{A_1}} + N_{\mathrm{A_T}} + N_{\mathrm{A_2}} + N_{\mathrm{B}}$ segments in total with $N_{\mathrm{A_1}} = N_{\mathrm{A_1'}} + N_{\mathrm{A_1,stiff}}$, $N_{\mathrm{A_2}} = N_{\mathrm{A_2'}} + N_{\mathrm{A_2,stiff}}$ and $N_{\mathrm{A_T}} = N_{\mathrm{A_T'}} + N_{\mathrm{A_T,stiff}}$, where $N_{\mathrm{A_1,stiff}}$, $N_{\mathrm{A_2,stiff}}$ and $N_{\mathrm{A_T,stiff}}$ are the number of stiffened segments on the A_1-, A_2- and A_T- blocks, respectively. We set that $N_{\mathrm{A_T}} = 2N_{\mathrm{A_T,stiff}}$ and $N_{\mathrm{A_1,stiff}} = N_{\mathrm{A_2,stiff}} = N_{\mathrm{A_T,stiff}}$. Therefore, the total volume fraction of the stiffened segment is $f_{\mathrm{A,stiff}} = f_{\mathrm{A_1,stiff}} + f_{\mathrm{A_2,stiff}} + f_{\mathrm{A_T,stiff}} = N_{\mathrm{A_1,stiff}}/N + N_{\mathrm{A_2,stiff}}/N + N_{\mathrm{A_T,stiff}}/N = 3f_{\mathrm{A_T,stiff}} = \frac{3}{2} f_{\mathrm{A_T}}$, and the volume fractions of the remainder of the A-blocks are $f_{\mathrm{A_1'}} = N_{\mathrm{A_1'}}/N$, $f_{\mathrm{A_2'}} = N_{\mathrm{A_2'}}/N$, and $f_{\mathrm{A_T'}} = N_{\mathrm{A_T'}}/N$. The only difference between the stiffened A-segments and the other A-segments is the statistical segment length. We set the statistical segment length of the stiffened A-segments to be $b_{\mathrm{A,stiff}}/b_{\mathrm{B}} = 2.5$. This model system is denoted model II. The following lists the propagators on a modified $A_1A_TA_2$-B branched block copolymer chain and their initial conditions:

Propagator	block	α	Initial Condition
$q_{0,1}(\mathbf{r},s)$	$\mathrm{A_1'}$	A	$q_{0,1}(\mathbf{r},s=0)=1$
$q_{4,3}(\mathbf{r},s)$	$\mathrm{A_T'}$	A	$q_{4,3}(\mathbf{r},s=0)=1$
$q_{7,6}(\mathbf{r},s)$	B	B	$q_{7,6}(\mathbf{r},s=0)=1$
$q_{1,2}(\mathbf{r},s)$	$\mathrm{A_{1,stiff}}$	A	$q_{1,2}(\mathbf{r},s=0)=q_{0,1}(\mathbf{r},s=1)$
$q_{3,2}(\mathbf{r},s)$	$\mathrm{A_{T,stiff}}$	A	$q_{3,2}(\mathbf{r},s=0)=q_{4,3}(\mathbf{r},s=1)$
$q_{2,5}(\mathbf{r},s)$	$\mathrm{A_{2,stiff}}$	A	$q_{2,5}(\mathbf{r},s=0)=q_{1,2}(\mathbf{r},s=1)q_{3,2}(\mathbf{r},s=1)$

$q_{5,6}(\mathbf{r},s)$	A_2'	A	$q_{5,6}(\mathbf{r},s=0)=q_{2,5}(\mathbf{r},s=1)$
$q_{6,7}(\mathbf{r},s)$	B	B	$q_{6,7}(\mathbf{r},s=0)=q_{5,6}(\mathbf{r},s=1)$
$q_{6,5}(\mathbf{r},s)$	A_2'	A	$q_{6,5}(\mathbf{r},s=0)=q_{7,6}(\mathbf{r},s=1)$
$q_{5,2}(\mathbf{r},s)$	$A_{2,\mathrm{stiff}}$	A	$q_{5,2}(\mathbf{r},s=0)=q_{6,5}(\mathbf{r},s=1)$
$q_{2,3}(\mathbf{r},s)$	$A_{T,\mathrm{stiff}}$	A	$q_{2,3}(\mathbf{r},s=0)=q_{5,2}(\mathbf{r},s=1)q_{1,2}(\mathbf{r},s=1)$
$q_{2,1}(\mathbf{r},s)$	$A_{1,\mathrm{stiff}}$	A	$q_{2,1}(\mathbf{r},s=0)=q_{5,2}(\mathbf{r},s=1)q_{3,2}(\mathbf{r},s=1)$
$q_{3,4}(\mathbf{r},s)$	A_T'	A	$q_{3,4}(\mathbf{r},s=0)=q_{2,3}(\mathbf{r},s=1)$
$q_{1,0}(\mathbf{r},s)$	A_1'	A	$q_{1,0}(\mathbf{r},s=0)=q_{2,1}(\mathbf{r},s=1)$

The volume-fraction fields for A- and B-segments are given by

$$\begin{aligned}\phi_A(r)=&\int_0^1 dsq_{0,1}(r,s)q_{1,0}(r,N-s)+\int_0^1 dsq_{1,2}(r,s)q_{2,1}(r,N-s)\\&+\int_0^1 dsq_{2,3}(r,s)q_{3,2}(r,N-s)+\int_0^1 dsq_{3,4}(r,s)q_{4,3}(r,N-s),\\&+\int_0^1 dsq_{2,5}(r,s)q_{5,2}(r,N-s)+\int_0^1 dsq_{5,6}(r,s)q_{6,5}(r,N-s)\end{aligned}\tag{S4}$$

and

$$\phi_{\mathrm{B}}(\mathbf{r})=\int_0^1 \mathrm{d}sq_{3,4}(\mathbf{r},s)q_{4,3}(\mathbf{r},N-s).$$

We use model II to calculate the bulk periodicity for HEX phase only, the other SCF calculations are performed using model I. We solve the MDEs using the 4[th]-order Richardson-extrapolated pseudo-spectral method and the integration over s is computed numerically via 4[th]-order Romberg integration[1], with chain contour discretization $\Delta\tilde{s}=0.001$. The spatial discretization $n_{\mathbf{r}}$ is $128^2\times64$ for FK s phase, 64^3 for BCC and FK A15 phases, and 64^2 for HEX. The SCF equations are solved iteratively with the Helmholtz free energy being minimized simultaneously using Anderson mixing[2, 3]. All SCF calculations in this work are performed using the open-source program PSCF+[4].

5. Supplementary calculation and discussion

5.1Volume fraction of total LA (f_L)

The volume fraction of the total LA component (f_L) in the blends is calculated by Eq. S5:

$$f_L = \frac{M_L/\rho_L}{M_L/\rho_L + M_D/\rho_D} \tag{S5}$$

where ω_H is the mass fraction of the homopolymer in the blend; M_L and M_D are the molecular weight of *o*LA and *o*DA blocks; ρ_L and ρ_D are the density of *o*LA and *o*DA blocks, respectively. According to literature, ρ_L = 1.25 g/cm^3, ρ_D = 0.95 g/cm^3. For the neat block copolymer, ω_H = 0.

5.2 characteristic dimension of phase (*a*)

The dimension of phase (*a*) refers to inter-column distance (for HEX), or lattice parameters (for σ and BCC), it can be calculated from corresponding diffraction peaks accordingly.

$$a = 2d_{10}/\sqrt{3} \qquad \text{for HEX}$$

$$a = \sqrt{2}d_{110} \qquad \text{for BCC} \tag{S6}$$

$$a = \sqrt{17}d_{410};\ \ c = 2d_{002} \qquad \text{For } \sigma \text{ phase}$$

5.3 Average diameter of spherical motifs of σ phases (D)

$$D = \sqrt[3]{\frac{3}{\pi}a} \qquad \text{for BCC} \tag{S7}$$

$$D = \sqrt[3]{\frac{V}{5\pi}} \qquad \text{For } \sigma \text{ phase}$$

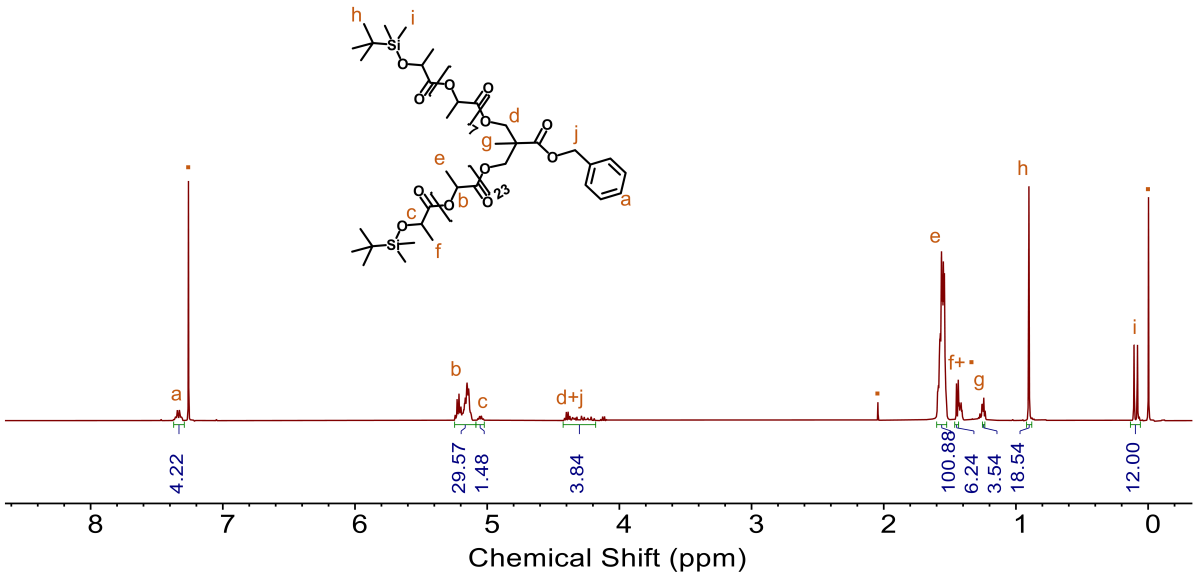
5.4 Index of peaks in the SAXS pattern of $L_{32}(L_8)$-DA_{24} (σ phase)

Peak No.	(*hkl*)	$q_{cal.}$ (nm^{-1})	$q_{obs.}$ (nm^{-1})	Peak No.	(*hkl*)	$q_{cal.}$ (nm^{-1})	$q_{obs.}$ (nm^{-1})
1	110	0.2056		**21**	420	0.6503	
2	200	0.2908		**22**	411	0.6598	0.6590
3	101	0.3114		**23**	331	0.6756	
4	210	0.3251		**24**	222	0.6874	
5	111	0.3437		**25**	421	0.7061	
6	220	0.4113		**26**	312	0.7174	0.7170
7	211	0.4260		**27**	430	0.7270	
8	310	0.4616	0.4616	**28**	510	0.7414	
9	221	0.4950		**29**	322	0.7603	
10	301	0.5159		**30**	501	0.7774	
11	320	0.5243		**31**	431	0.7774	
12	311	0.5360		**32**	520	0.7831	
13	002	0.5507	0.5507	**33**	511	0.7908	0.7904
14	400	0.5816		**34**	402	0.8010	
15	112	0.5886		**35**	412	0.8140	
16	321	0.5922		**36**	440	0.8225	
17	410	0.5996	0.6009	**37**	332	0.8270	
18	330	0.6169	0.6231	**38**	521	0.8301	
19	202	0.6228	0.6231	**39**	103	0.8388	
20	212	0.6395	0.6396				

5.5 Index of peaks in the SAXS pattern of L_{40}-DA_{32} (σ phase)

Peak No.	(*hkl*)	$q_{cal.}$ (nm^{-1})	$q_{obs.}$ (nm^{-1})	Peak No.	(*hkl*)	$q_{cal.}$ (nm^{-1})	$q_{obs.}$ (nm^{-1})
1	110	0.1898		**21**	420	0.6003	
2	200	0.2684		**22**	411	0.6090	0.6114
3	101	0.2874		**23**	331	0.6235	

4	210	0.3001		**24**	222	0.6344	
5	111	0.3172		**25**	421	0.6518	
6	220	0.3796		**26**	312	0.6622	
7	211	0.3932		**27**	430	0.6711	0.6729
8	310	0.4245	0.4245	**28**	510	0.6843	
9	221	0.4569		**29**	322	0.7018	
10	301	0.4762		**30**	501	0.7175	
11	320	0.4839		**31**	431	0.7175	
12	311	0.4947		**32**	520	0.7228	
13	002	0.5083	0.5081	**33**	511	0.7299	
14	400	0.5368		**34**	402	0.7393	0.7410
15	112	0.5432		**35**	412	0.7514	
16	321	0.5466		**36**	440	0.7592	
17	410	0.5534		**37**	332	0.7633	
18	330	0.5694	0.5697	**38**	521	0.7662	
19	202	0.5748	0.5763	**39**	103	0.7742	
20	212	0.5903					



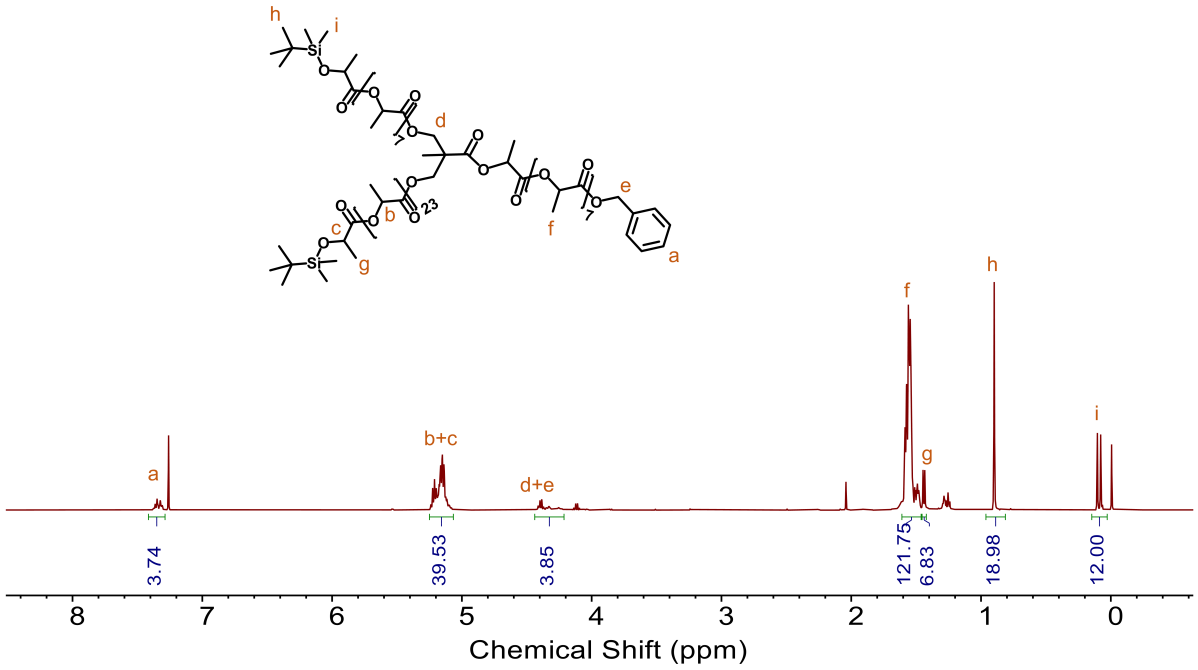


Figure S1. ^{1}H NMR spectra of the A block.

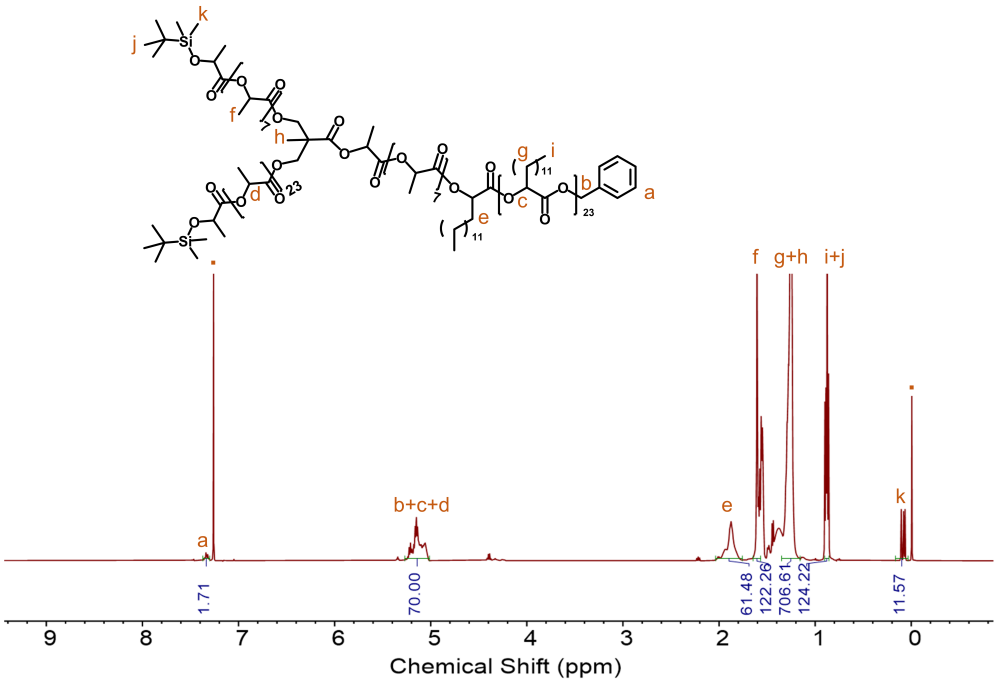


Figure S2. ^{1}H NMR spectra of the A-B Block.

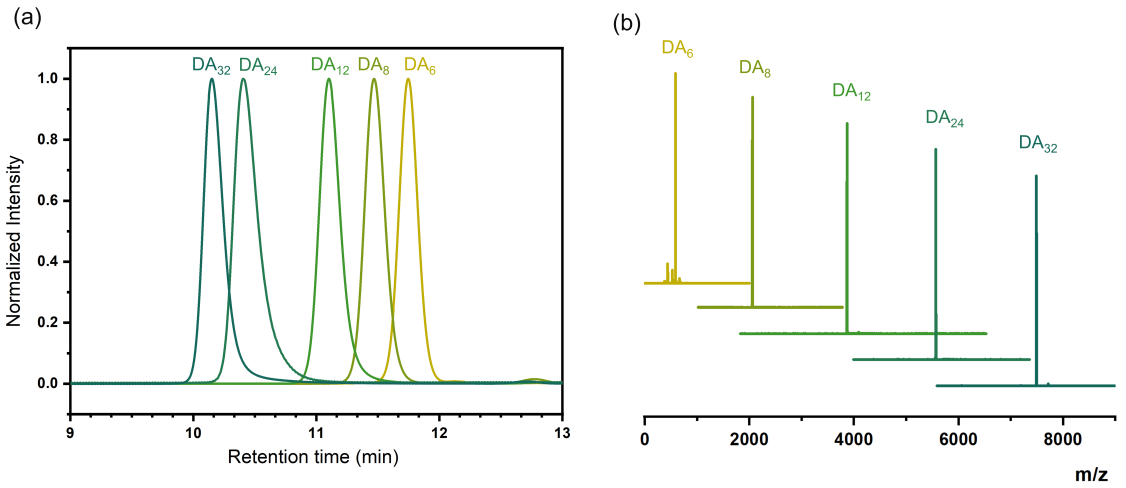


Figure S3. SEC traces (a) and MALDI ToF MS data (b) of the homopolymer *o*LA library.

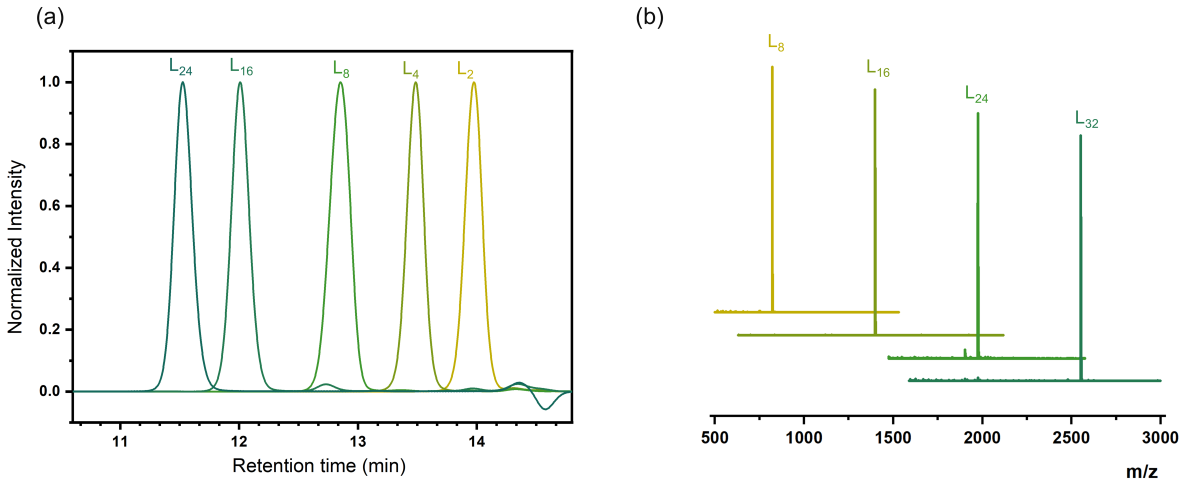


Figure S4. SEC traces (a) and MALDI ToF MS data (b) of the homopolymer *o*DA library.

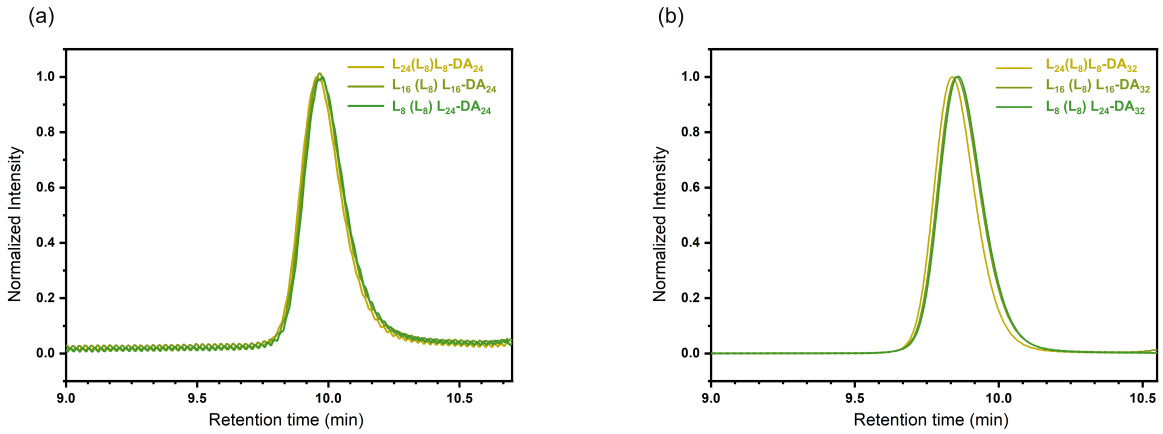


Figure S5. SEC elution traces of $DA_{24}L_{40}$ and $DA_{32}L_{40}$.

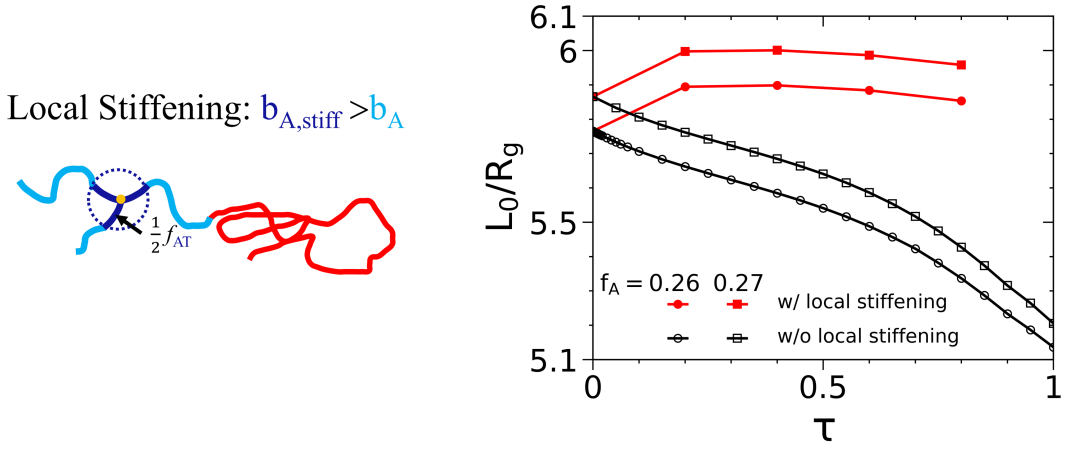


Figure S6. (a) Local Stiffening at the grafting point. (b) Bulk periodicity L_0 in the unit of the radius of gyration $R_g \equiv \sqrt{\frac{N}{6}}b$ as a function of τ for HEX phase, comparing models with (red) and without (black) local stiffening. $f_{A,stiff}$=3×0.5×f_{AT}, χN=25, b_A/b_B=1.84 and $b_{A,stiff}/b_B$=2.5.

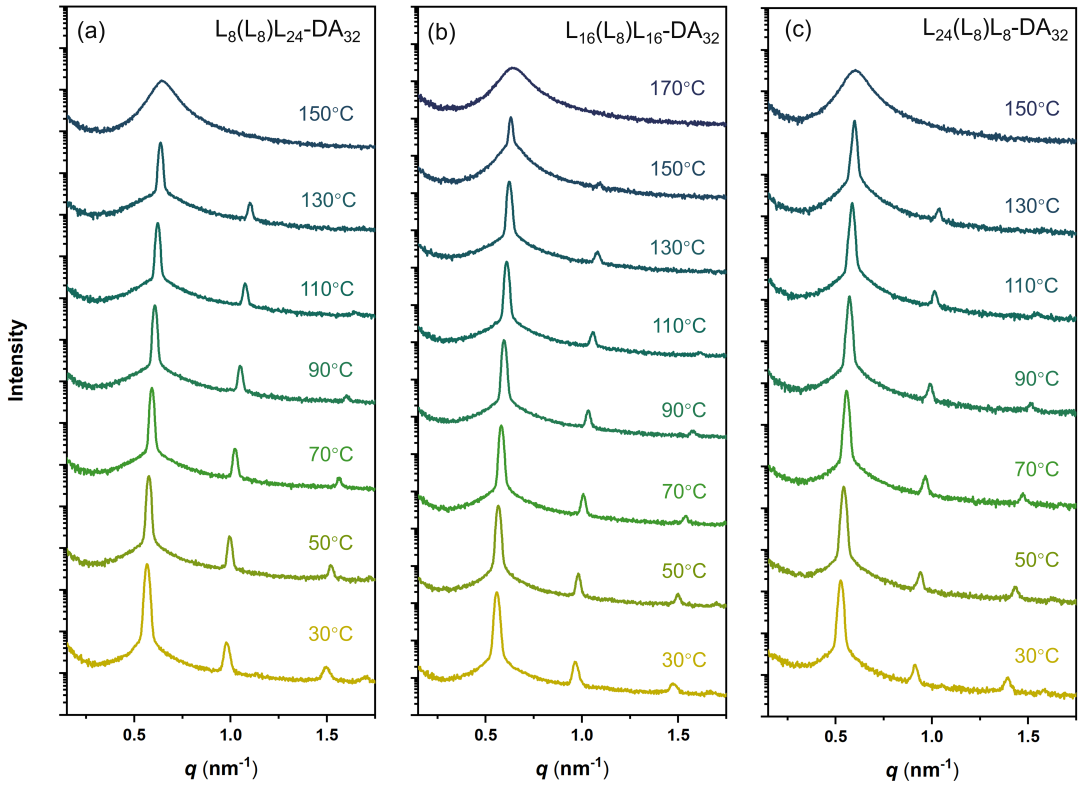


Figure S7. *In-situ* temperature dependent SAXS profiles of the library of $L_{40}DA_{24}$.

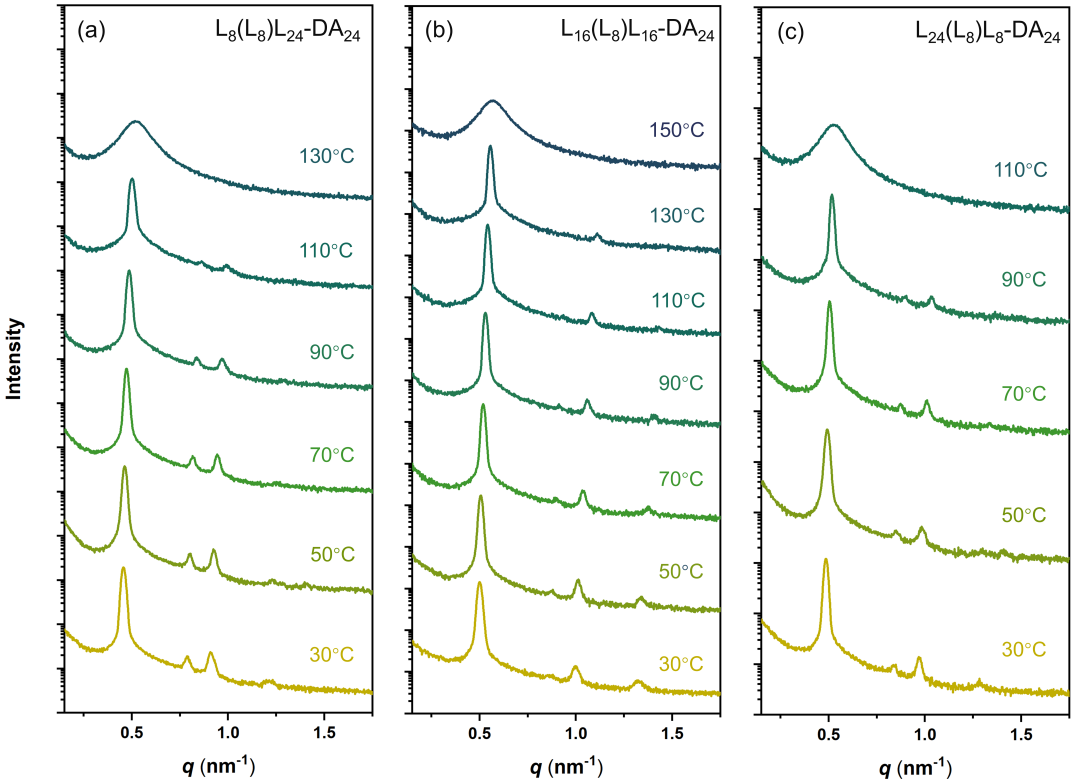


Figure S8. *In-situ* temperature dependent SAXS profiles of the Library of $L_{40}DA_{32}$.

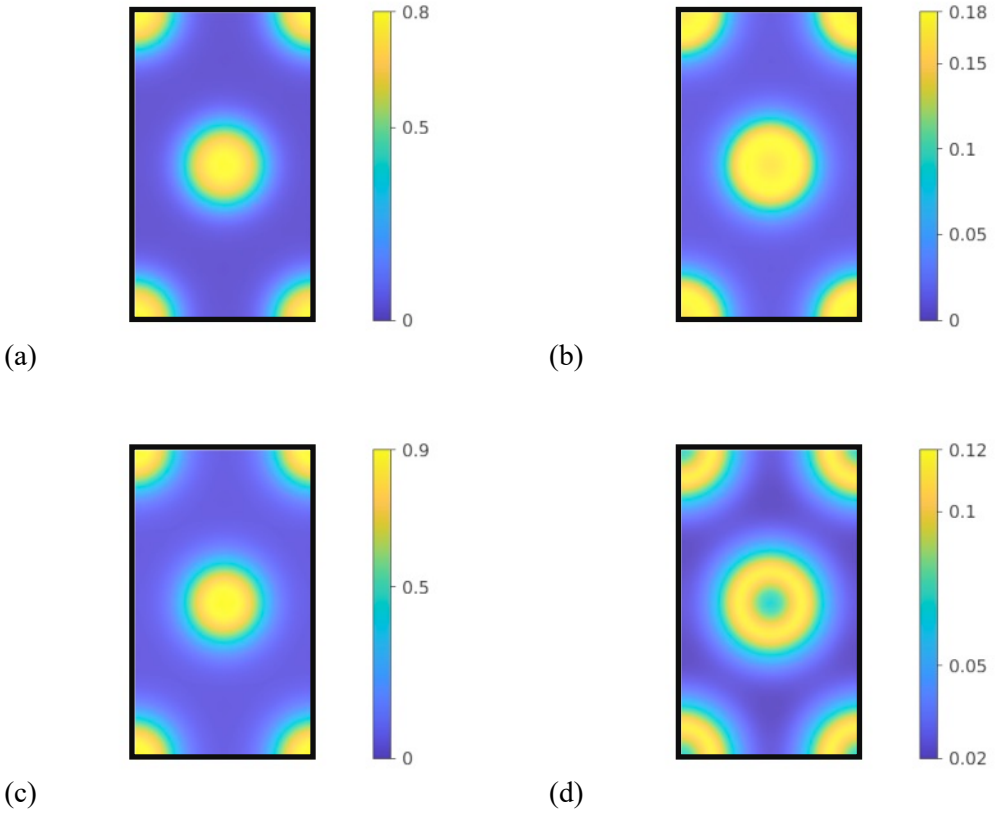


Figure S9. Volume fraction field of A-segments on (a) A_1-block, $\phi_{A_1}(\mathbf{r})$, and (b) A_T-block, $\phi_{A_T}(\mathbf{r})$, at τ = 0.8. (c) $\phi_{A_1}(\mathbf{r})$ and (d) $\phi_{A_T}(\mathbf{r})$ at $\tau = 1$. HEX, f_A=0.26, χN=25, and $b_A/b_B = 1.84$.

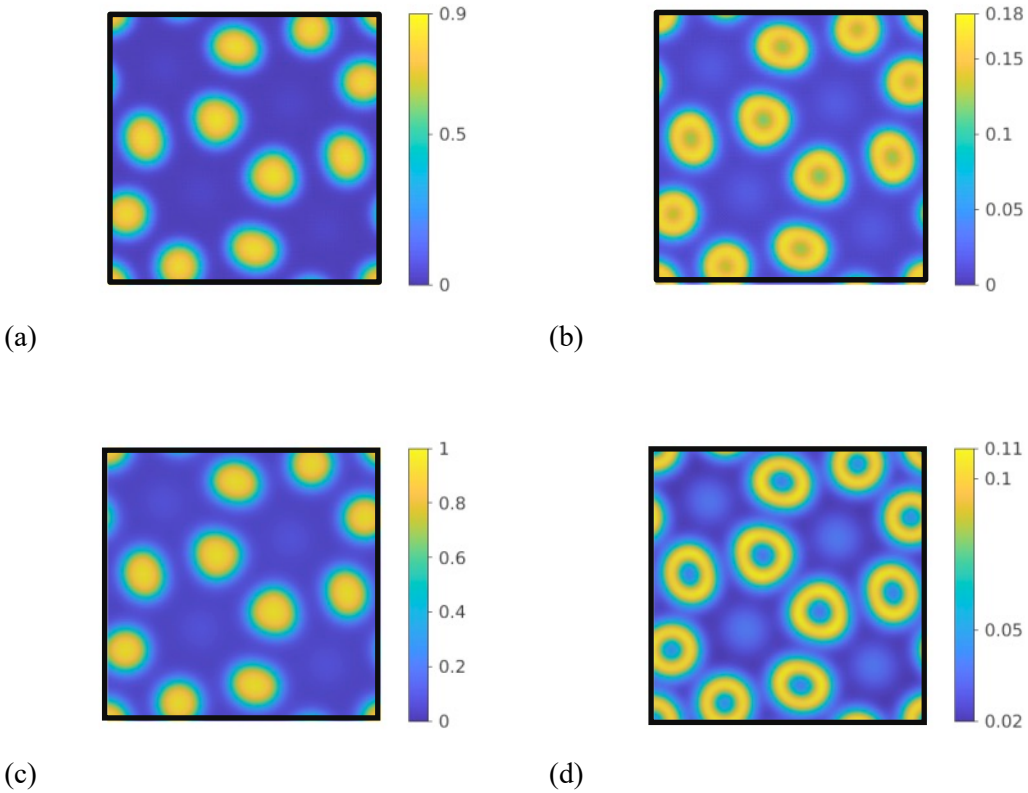


Figure S10. Volume fraction field of A-segments on (a) A_1-block, $\phi_{A_1}(\mathbf{r})$, and (b) A_T-block, $\phi_{A_T}(\mathbf{r})$, at τ = 0.8. (c)

$\phi_{A_1}(\mathbf{r})$ and (d) $\phi_{A_T}(\mathbf{r})$ at τ = 1. FK σ [the (001) plane], f_A=0.26, χN=25, and b_A/b_B=1.84.

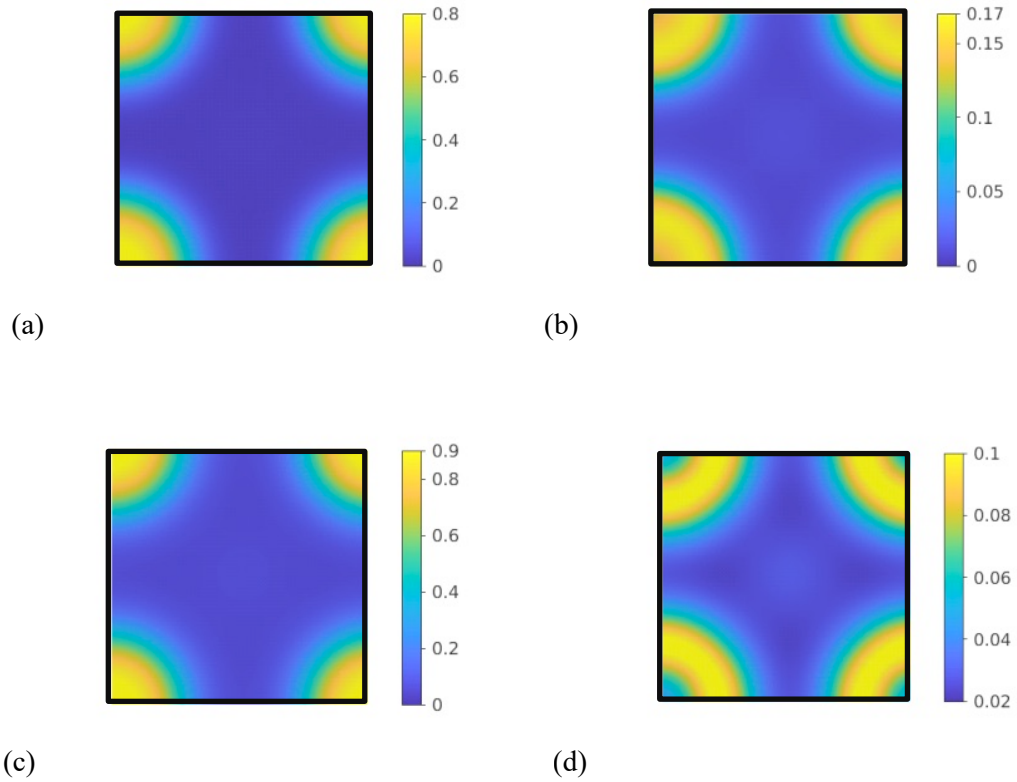


Figure S11. Volume fraction field of A-segments on (a) A_1-block, $\phi_{A_1}(\mathbf{r})$, and (b) A_T-block, $\phi_{A_T}(\mathbf{r})$, at τ = 0.8. (c) $\phi_{A_1}(\mathbf{r})$ and (d) $\phi_{A_T}(\mathbf{r})$ at τ = 1. BCC [the (001) plane],, f_A=0.26, χN=25, and b_A/b_B=1.84.

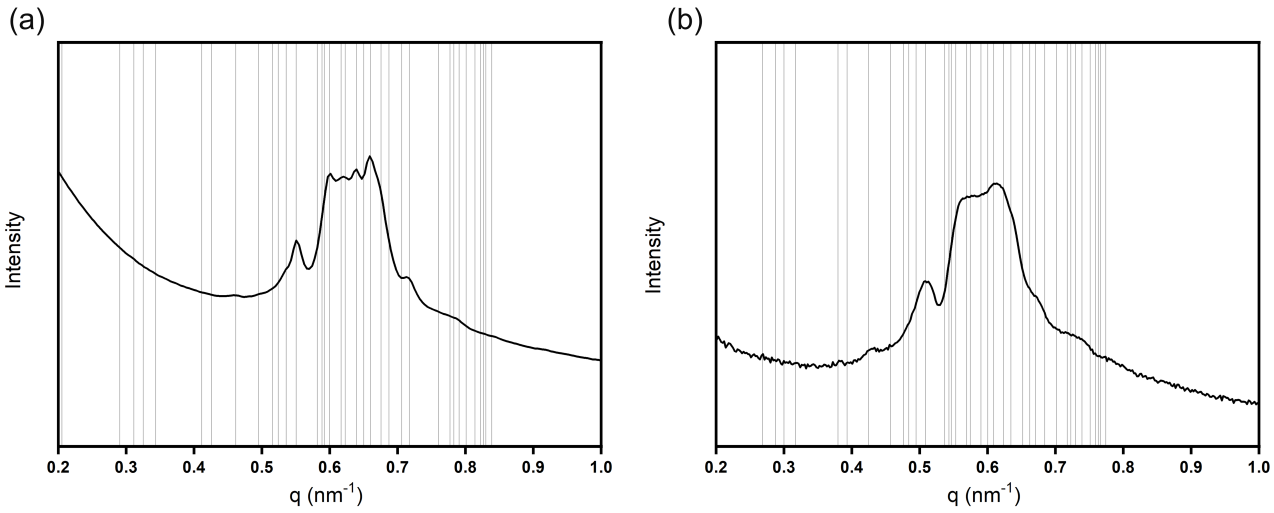


Figure S12. Peaking indexing of 1D SAXS profiles of (a) $(L_8)L_{32}$-DA_{24}, (b) $L_{40}DA_{32}$ (σ phase). Droplines are the allowed reflections based on the calculated lattice parameter.

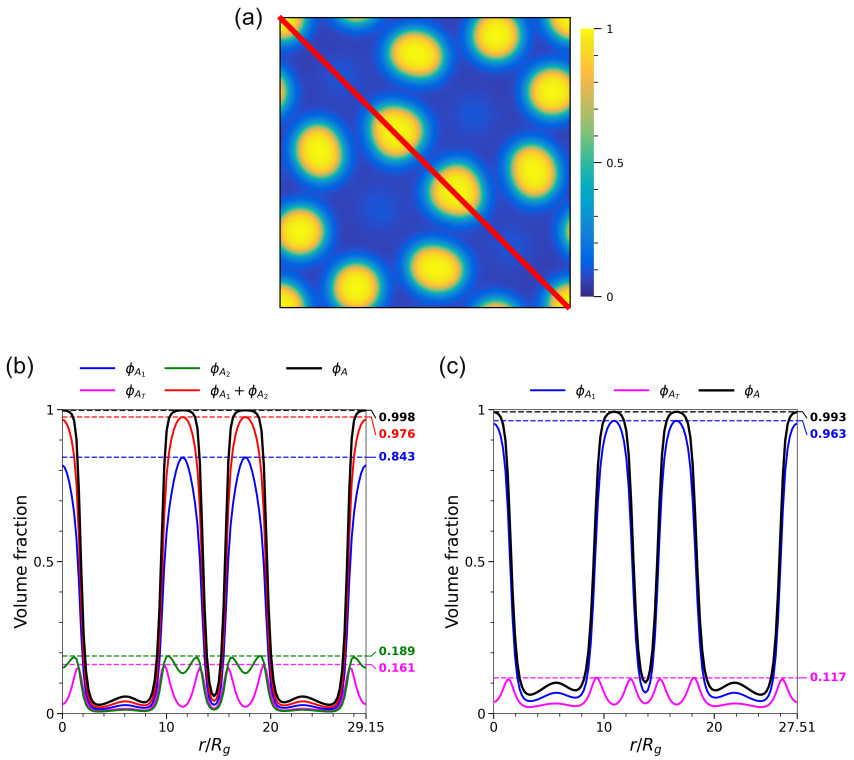


Figure S13. (a) Volume-fraction field of A-segment for the FK σ phase in the direction of [001] at f_A=0.26. The decomposition of volume-fraction field of A-segment into A_1-, A_2- and A_T-block contributions at (b) τ = 0.75 and (c) τ = 1 along the red line as shown in (a).

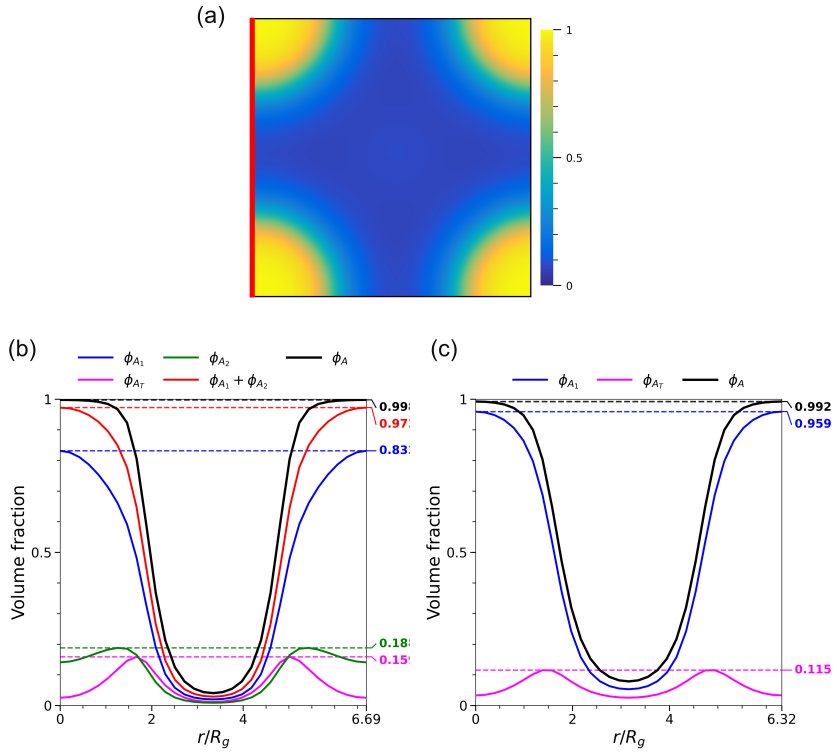


Figure S14. (a) Volume-fraction field of A-segment for the BCC phase in the direction of [001] at f_A=0.26, χN=25, and b_A/b_B=1.84. The decomposition of volume-fraction field of A-segment into A_1-, A_2- and A_T-block

contributions at (a) τ=0.75 and (b) τ=1 along the red line as shown in (a).

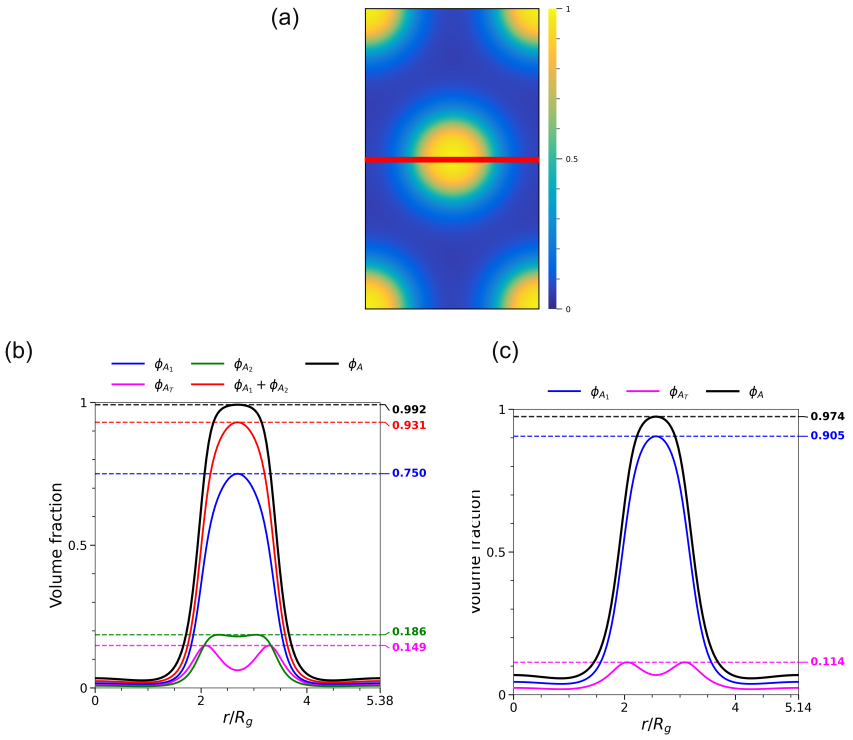


Figure S15. (a) Volume-fraction field of A-segment for the HEX phase at f_A=0.26, χN=25, and b_A/b_B=1.84. The decomposition of volume-fraction field of A-segment into A_1-, A_2- and A_T-block contributions at (a) τ=0.75 and (b) τ=1 along the red line as shown in (a).

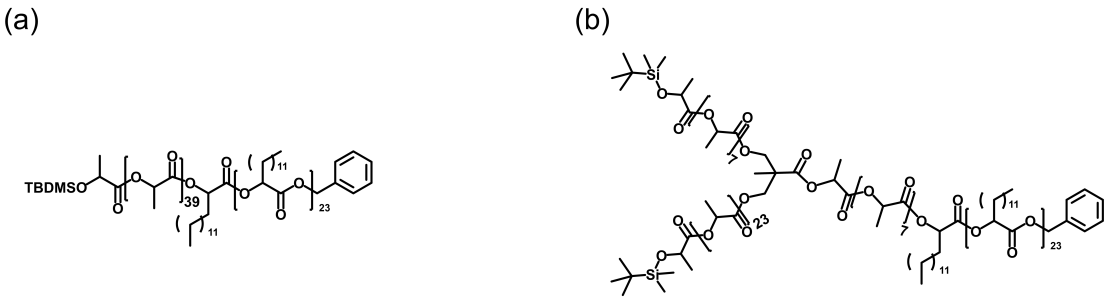


Figure S16. Chemical structures of $L_{40}DA_{24}$ with different topological architectures: (a) linear and (b) branched polymers."

References

(1) Ma, Z.; Zhou, D.; Xu, M.; Gan, Z.; Zheng, T.; Wang, S.; Tan, R.; Dong, X.-H. Discrete Linear–Branched

Block Copolymer with Broken Architectural Symmetry. *Macromolecules* **2023**, 56, 833-840.

(2) Press, W. H. Numerical recipes in C: *The art of scientific computing*; Cambridge University Press, 1992.

(3) Matsen, M. W. Fast and accurate SCFT calculations for periodic block-copolymer morphologies using the spectral method with Anderson mixing. *Eur. Phys. J. E* **2009**, 30 (4), 361-369.

(4) Arora, A.; Morse, D. C.; Bates, F. S.; Dorfman, K. D. Accelerating self-consistent field theory of block polymers in a variable unit cell. *Journal of Chemical Physics* **2017**, 146 (24),

(5) *https://github.com/qwcsu/pscfplus.*